Stefan Leitner

Internal Model–Based Control Strategies for Voltage Source Converters

Master's Thesis

Submitted in Partial Fulfillment of the Requirements for the Degree of

Diplom Ingenieur
(Dipl.-Ing.)

in
Electrical Engineering

at

Graz University of Technology

In Cooperation with
Washington State University, Pullman, WA, USA

Univ.-Prof. Dr.-Ing. Annette Mütze
Electric Drives and Machines Institute
Graz University of Technology

2016

Statutory Declaration

I declare that I have authored this thesis independently, that I have not used other than the declared sources/resources, and that I have explicitly marked all material which has been quoted either literally or by content from the used sources.

Graz, _____

Date Signature

Eidesstattliche Erklärung

Ich erkläre an Eides statt, dass ich die vorliegende Arbeit selbstständig verfasst, andere als die angegebenen Quellen/Hilfsmittel nicht benutzt, und die den benutzten Quellen wörtlich und inhaltlich entnommenen Stellen als solche kenntlich gemacht habe.

Graz, _____

Datum Unterschrift

Contents

Thesis Outline

Within the framework of this thesis, advanced control strategies of voltage source converters in microgrids are developed, discussed, and analyzed in detail. Therefore, both the islanded and grid-connected operating modes of the microgrid are investigated in two separate studies. In either case, the focus is on the controlled injection of power by the voltage source converter into the microgrid and/or main grid. Internal model–based control strategies are developed, utilized, and analyzed and in turn compared with common control practices.

This thesis encompasses three major parts:

- Part I, with the title *General*, introduces the concepts of microgrid, *dq* reference frame, linearization of sets of non-linear differential-algebraic equations, and internal model control, necessary to fully comprehend the material presented in Part II and Part III of this thesis.

- Part II, with the title *Small-Signal Stability Analysis of an Inverter-Based Microgrid with Internal Model–Based Controllers*, deals with state-space modeling and eigenvalue analysis of current and voltage controllers of voltage source converters incorporated in an islanded microgrid. It builds upon the work of Dr. Mehrdad Yazdanian and Dr. Ali Mehrizi-Sani [1–3]. The findings of Part II have been submitted to *IEEE Transactions on Power Systems* as Leitner *et al.* [4].

- Part III, with the title *Internal Model–Based Active Damping Current Control for a Grid-Connected Voltage Source Converter with an LCL Filter*, proposes a novel internal model–based current controller for active resonance damping of an LCL filter. The findings of Part III have been submitted to *IEEE Transactions on Power Delivery* as Leitner *et al.* [5].

The study was conducted at Washington State University, Pullman, WA, USA, in cooperation with Graz University of Technology, Graz, Austria. The research was supported in part by the Austrian Marshall Plan Foundation through scholarship number 639 848 22 15 2015.

Acknowledgements

A major chapter of my life has drawn to a close. Undoubtedly, this chapter was full of both adventures and hard work and I would like to seize the moment and express my deepest gratitude to all the people who supported me during this journey full of learning and personal development.

First of all, I would particularly like to thank my advisor Univ.-Prof. Dr.-Ing. Annette Mütze at Graz University of Technology, Graz, Austria. She was the one who initiated this project and if it was not for her support and guidance, this thesis would have not been possible. I am greatly indebted to Ass.-Prof. Dr. Ali Mehrizi-Sani at Washington State University, Pullman, WA, USA, for incorporating me into his research team and being very tolerant and supportive throughout this project. I would also like to express my deepest appreciation to my friend and colleague Dr. Mehrdad Yazdanian, who I worked with the closest and from whose experience I have greatly benefited. Special thanks go to the Austrian Marshall Plan Foundation for their financial support of my stay at Washington State University, Pullman, WA, USA, which was academically the best thing that ever happened to me. I would also like to thank the International Student Exchange Program (ISEP) and the University of Tennessee, Knoxville, TN, USA, for making possible my academic year 2014/15, which broadened my horizons in many ways and probably was the best experience of my life. Last but not least, I would like to offer my special thanks to my parents, relatives, and friends in Austria and all over the world for their endless support and encouragement.

Abstract

Microgrids provide an effective means for the integration of distributed energy resources (DER) in the power grid. Commonly, power electronic converters, e.g., voltage source converters (VSC), serve as an interface between the distributed generation (DG) and the grid. While extensive research has already been conducted on control strategies for VSCs, there are still gaps in improving their stability, transient behavior, and power quality, especially when it comes to dealing with resonance phenomenons which can jeopardize the system stability.

This thesis is divided into three major parts:

- Part I serves as an introduction to microgrid, *dq* reference frame, linearization, and internal model control.

- Part II studies the performance of cascade internal model–based current and voltage control loops by deriving a state-space small-signal model and performing eigenvalue analysis on an islanded inverter-based microgrid system. The results are compared with those of the same system but with conventional proportional-integral (PI)-based current and voltage controllers. Simulation case studies are performed in PSCAD/EMTDC environment to compare the transient behavior of both methods. The results confirm the superior performance of the internal model–based controllers. Compared with PI-based controllers, the characteristic behavior of internal model–based voltage and current controllers includes 1) increased damping ratios and frequencies of sensitive eigenvalues, 2) increased robustness against parameter changes, 3) faster step response, and 4) reduced over/undershoot in current and voltage transients.

- Part III proposes a novel active damping current controller based on the internal model principle for grid-connected VSCs integrated with LCL filters for the reduction of switching current ripples. The controller can be considered a high-order multi-input multi-output (MIMO) filter, implemented in the *dq*

reference frame, including decoupling terms for improved transient behavior. Simulation case studies are performed in PSCAD/EMTDC environment to ratify the controller's functionality, evaluate the transient behavior, and test its robustness against parameter changes. The results are compared with those of two existing active damping strategies. The study confirms the superior performance of the proposed internal model–based active damping current controller which shows 1) improved transient behavior, 2) increased robustness against parameter changes, and 3) simpler tuning compared with existing control strategies for active resonance damping of LCL filters.

Zusammenfassung

Inselnetze, die sowohl autonom wie auch im Verbundbetrieb mit dem übergeordneten Netz operieren können, werden als *Microgrids* bezeichnet. Ein *Microgrid* kann als eine Akkumulation dezentraler Energieerzeuger und -speichermöglichkeiten in unmittelbarer Nähe von Verbrauchern gesehen werden. Sie bieten eine gute Möglichkeit, dezentrale Erzeugungsanlagen ins Stromnetz zu integrieren. Bindeglied ist meist ein leistungselektronischer Konverter (z.B. *Voltage Source Converter*), für dessen Regelung bereits eine große Bandbreite an verschiedenen Reglerkonzepten entwickelt wurde. Jedoch gibt es noch immer Verbesserungspotenzial, was die Stabilität, das transiente Verhalten und die Qualität der gelieferten Energie angeht, insbesondere da unter bestimmten Umständen Resonanzerscheinungen auftreten können, die die Systemstabilität erheblich gefährden können.

Die vorliegende Masterarbeit ist in drei Teile eingeteilt:

- Teil I erklärt den Begriff *Microgrid* und widmet sich den Themen Linearisierung, rotierende Koordinatensysteme und *Internal Model Control*.

- Teil II umfasst die Entwicklung von Kleinsignalzustandsraummodellen für kaskadierte Strom- und Spannungsregler, die auf dem *Internal Model*–Prinzip basieren. Diese werden in weiterer Folge in das Kleinsignalzustandsraummodel eines Test-*Microgrids* integriert, um mit der resultierenden Systemmatrix Eigenwertanalysen durchzuführen und Aussagen über die Stabilität treffen zu können. Die Ergebnisse werden mit jenen von konventionellen *proportional-integral* (PI)-basierten Strom- und Spannungsreglern verglichen. Darüber hinaus werden mit dem Computerprogramm *PSCAD* Simulationen im Zeitbereich durchgeführt, um die untersuchten Reglerstrukturen auf ihr transientes Verhalten zu prüfen. Die Ergebnisse bestätigen das überlegene Verhalten der untersuchten Strom- und Spannungsregler, die auf dem *Internal Model*–Prinzip basieren. Verglichen mit PI-basierten Reglern, Strom- und Spannungsregler die auf dem *Internal Model*–Prinzip basieren zeigen 1) erhöhte Frequenzen und

Dämpfungsmaße kritischer Eigenwerte, 2) höhere Robustheit gegen Parametervariationen, 3) schnellere Sprungantworten und 4) reduziertes Über- und Unterschwingen der transienten Strom- und Spannungsverläufe.

- Teil III beinhaltet die Entwicklung einer neuartigen Reglerstruktur, basierend auf dem *Internal Model*–Prinzip, zur aktiven Dämpfung von Resonanzerscheinungen die bei *Voltage Source Converter* im Zusammenhang mit LCL-Filter zur Stromglättung auftreten können. Der vorgeschlagene Regler kann als *multi-input multi-output* (MIMO) Filter höherer Ordnung angesehen werden, dessen Modellierung in einem rotierenden Koordinatensystem erfolgt, einschließlich Kopplungsterme, die das transiente Verhalten verbessern sollen. Simulationen im Zeitbereich mittels *PSCAD* werden herangezogen, um die Wirksamkeit und Robustheit des Reglers zu testen. Der entwickelte Regler wird mit zwei ausgewählten bereits etablierten Regelstrategien zur aktiven Resonanzdämpfung verglichen. Die Untersuchungen zeigen, dass der entwickelte Regler erhebliche Vorteile im Hinblick auf 1) transientes Verhalten, 2) Robustheit und 3) Einfachheit des Reglertunings gegenüber existierenden Regelstrategien für diese Anwendung aufweist.

Keywords

Active resonance damping, current control, distributed power generation, eigenvalues, grid-connected microgrid, internal model control, islanded microgrid, inverter, LCL filter, sensitivity analysis, small-signal stability, state-space model, voltage control, voltage source converter.

Part I

General

Chapter 1

Microgrid

The following three sections deal with the concept of microgrid including its definition, control structure, and challenges faced.

1.1 Introduction

For the most part, today's power grids were built decades ago and were designed to have fewer but larger central generating stations which are easy to manage and control. Beside a steady increase in power demand, the utilization of distributed energy resources (DER) is, due to the high number of small-scale distributed generation (DG) units and their distributed nature, accompanied by several challenges for the conventional power grid. That is why currently the trend is toward smart gird, as an intelligent electric network, including enhanced employment of communication and automation technology, to ensure a safe, reliable but also efficient operation of the grid.

Microgrids can be considered main building blocks of a smart grid and can help integrate DG units into the grid, improving thereby the power grid's reliability and sustainability. A microgrid is a single controllable entity and defined as a collection of DG and distributed storage units in close proximity of the loads [6].

A microgrid can operate in both grid-connected and islanded operating modes [7–9]. In the grid-connected mode, the voltage and frequency are dictated by the main grid. However, in the islanded mode, the controllers of the DG units in the microgrid are responsible for regulation of voltage and frequency and for power sharing between DG units [10–13].

1.2 Microgrid Control Structure

In order to guarantee a safe, reliable, and efficient operation, a functioning microgrid control structure is inevitable. The principal roles of the microgrid control structure are [11]:

- Voltage and frequency regulation;
- Proper load sharing and DER coordination;
- Microgrid resynchronization with the main grid;
- Power flow control between the microgrid and the main grid;
- Optimizing the microgrid operating costs.

These requirements are of different significance and time scales. That is why the hierarchical control strategy consists of four levels, namely, zero-level, primary, secondary, and tertiary controls [11]:

- *Zero-level control* consists of inner current and outer voltage control loops and is responsible for output current and voltage regulation of the DG unit;
- *Primary control* provides set points for the *zero-level control* and is responsible for power sharing and voltage and frequency stabilization subsequent to load and generation changes;
- *Secondary control* compensates for the voltage and frequency deviations caused by the *primary control*; and
- *Tertiary control* manages the power flow between the microgrid and the main grid and facilitates an economically optimal operation.

Zero-level control shows the fastest dynamics followed by primary, secondary, and lastly tertiary control. This difference in time scale allows for individual designs of the four control levels.

1.3 Challenges

In conventional power systems, the rotating mass of large generators can compensate sudden imbalance between generation and consumption. As mentioned before, DG units such as fuel-cells, photovoltaics, and microturbines are often interfaced to the network through power electronic converters, which make the source more flexible in its operation and control compared to conventional electrical machines. However, inverter-based microgrids exhibit negligible physical inertia making them potentially prone to oscillations resulting from generation and load changes, and network disturbances [14]. In addition, these power electronic converters require output filters (L, LC, LCL, etc.) to decrease switching harmonics. High-order output filters (e.g., LCL filters) are economically advantageous for high-power applications but can also cause resonance problems that may jeopardize the stability of the system.

Ergo, improving voltage and current transients in microgrids and ensuring proper resonance damping are of utmost interest allowing for a more effective utilization of the electric power delivery infrastructure and also prevention of operation limit violations [3]. As a consequence, the stability margin of the microgrid can be increased.

Part II of this thesis studies the stability of internal model–based current and voltage controllers (i.e., zero-level controllers) proposed by [1, 3], by developing a small-signal state-space model which, in further consequence, is utilized for eigenvalue and sensitivity analysis of a test microgrid with three DG units, connected via two lines, and supplying two loads.

Part III of this thesis proposes an active damping current controller (i.e., zero-level controller) based on the internal model principle for grid-connected voltage source converters with LCL filters. The controller can be considered a high-order multi-input multi-output (MIMO) transfer function, implemented in the *dq* reference frame, including decoupling terms for improved transient behavior.

Chapter 2

Theoretical Background

The following sections are partly based on [15,16] and serve as a short introduction to rotating reference frames (RRF) and the linearization procedure utilized for the small-signal state-space modeling.

2.1 $dq0$ Reference Frame

As an extension of the Clark transform, the $dq0$ or Park transform is a space vector transformation of three-phase time-domain signals from a stationary phase coordinate system (ABC) to a rotating coordinate system ($dq0$) [15].

The following equation shows how the time-domain voltages u_a, u_b, and u_c transform into the $dq0$ reference frame where u_d is the direct-, u_q is the quadrature-, and u_0 is the zero-component:

$$\begin{bmatrix} u_d \\ u_q \\ u_0 \end{bmatrix} = \frac{2}{3} \begin{bmatrix} cos(\theta) & cos(\theta - \frac{2\pi}{3}) & cos(\theta + \frac{2\pi}{3}) \\ -sin(\theta) & -sin(\theta - \frac{2\pi}{3}) & -sin(\theta + \frac{2\pi}{3}) \\ \frac{1}{2} & \frac{1}{2} & \frac{1}{2} \end{bmatrix} \begin{bmatrix} u_a \\ u_b \\ u_c \end{bmatrix}, \tag{2.1}$$

where $\theta = \omega t$ and ω is the angular speed of the rotating reference frame.

The inverse transform is defined as follows:

$$\begin{bmatrix} u_a \\ u_b \\ u_c \end{bmatrix} = \begin{bmatrix} cos(\theta) & -sin(\theta) & 1 \\ cos(\theta - \frac{2\pi}{3}) & -sin(\theta - \frac{2\pi}{3}) & 1 \\ cos(\theta + \frac{2\pi}{3}) & -sin(\theta + \frac{2\pi}{3}) & 1 \end{bmatrix} \begin{bmatrix} u_d \\ u_q \\ u_0 \end{bmatrix}. \tag{2.2}$$

For balanced systems, i.e., sinusoidal current and voltage waveforms and system symmetry (same amplitudes and 120° phase shift between quantities), the zero-component is zero and can therefore be omitted.

The instantaneous output power $\tilde{s}$ of a DG unit can be calculated in the dq reference frame as follows:

$$\begin{aligned}\tilde{s} &= v i^* = (v_d + jv_q)(i_d + ji_q)^* = (v_d + jv_q)(i_d - ji_q) \\ &= i_d v_d - jv_d i_q + jv_q i_d + v_q i_d = \underbrace{(v_d i_d + v_q i_q)}_{\tilde{p}} + j\underbrace{(v_q i_d - v_d i_q)}_{\tilde{q}},\end{aligned} \tag{2.3}$$

where $\tilde{p}$, and $\tilde{q}$ are the instantaneous real and reactive power components of the instantaneous power $\tilde{s}$; and v_d, v_q, i_d, and i_q are the dq-components of the output voltage and current of the DG unit (v_o and i_o in Fig. 5.1).

The synchronous reference frame can be aligned to rotate with the voltage (e.g., voltage source converters) or with the current (e.g., current source converters). When it is aligned to the d-component of the voltage, the quadrature component $u_q = 0$. Ergo, the power equations reduce to:

$$\tilde{p} = u_d i_d \tag{2.4}$$

$$\tilde{q} = -u_d i_q. \tag{2.5}$$

Striking is the fact that now the real power $\tilde{p}$ solely depends on i_d while the reactive power $\tilde{q}$ solely depends on i_q. In other words, setting u_q to zero enables independent control of real and reactive power.

For balanced three-phase systems, the $dq0$ transform has the following advantageous characteristics [15]:

- The $dq0$ transform reduces three-phase AC quantities (e.g., u_a, u_b, and u_c) into two DC quantities (e.g., u_d, u_q). For balanced systems, the zero-component is zero. The DC quantities facilitate easier filtering and control.
- Active and reactive power can be controlled independently by controlling the dq-components.

2.2 Linearization Procedure

In general, the set of non-linear differential-algebraic equations are of the following form [16, 17]:

$$\dot{x} = f(x, \epsilon, u), \quad 0 = g(x, \epsilon, u), \quad y = h(x, \epsilon), \tag{2.6}$$

where x represents the state vector having n states, ϵ the r algebraic variables, u the m system input variables, and y the p output variables.

In steady state, time-derivates become zero ($\dot{x} = 0$) and the following set of equations results:

$$0 = f(x_0, \epsilon_0, u_0), \quad 0 = g(x_0, \epsilon_0, u_0), \quad y_0 = h(x_0, \epsilon_0). \tag{2.7}$$

This is the operating point (equilibrium) around which the system is to be linearized. Its neighborhood can then be described as:

$$x = x_0 + \Delta x, \quad \epsilon = \epsilon_0 + \Delta\epsilon, \quad u = u_0 + \Delta u, \quad y = y_0 + \Delta y. \tag{2.8}$$

Since small perturbations are assumed, the nonlinear function $y = h(x, \epsilon)$ in Equation 2.6 can be approximated by a first-order Taylor's series expansion. The ith of p outputs, y_i, then yields:

$$y_i = y_{i0} + \Delta y_i = h_i(x_0, \epsilon_0) + \frac{\partial h_i}{\partial x_1}\Delta x_1 + ... + \frac{\partial h_i}{\partial x_n}\Delta x_n + \frac{\partial h_i}{\partial \epsilon_1}\Delta\epsilon_1 + ... + \frac{\partial h_i}{\partial \epsilon_r}\Delta\epsilon_r, \tag{2.9}$$

where the partial derivatives $\frac{\partial h_i}{\partial x_a}$, $a = 1, ..., n$; and $\frac{\partial h_i}{\partial \epsilon_b}$, $b = 1, ..., r$; are evaluated at the initial steady state operating point (x_0, ϵ_0). Since $y_{i0} = h_i(x_0, \epsilon_0)$ in Equation 2.9, the linearized output equation reduces to:

$$\Delta y_i = \frac{\partial h_i}{\partial x_1}\Delta x_1 + ... + \frac{\partial h_i}{\partial x_n}\Delta x_n + \frac{\partial h_i}{\partial \epsilon_1}\Delta\epsilon_1 + ... + \frac{\partial h_i}{\partial \epsilon_r}\Delta\epsilon_r. \tag{2.10}$$

Applying a first-order Taylor's series expansion to the remaining non-linear equations in Equation 2.6 results in:

$$\Delta\dot{x}_j = \sum_{a=1}^{n} \frac{\partial f_j}{\partial x_a}\Delta x_a + \sum_{b=1}^{r} \frac{\partial f_j}{\partial \epsilon_b}\Delta\epsilon_b + \sum_{c=1}^{m} \frac{\partial f_j}{\partial u_c}\Delta u_c \tag{2.11}$$

and

$$0 = \sum_{a=1}^{n} \frac{\partial g_k}{\partial x_a}\Delta x_a + \sum_{b=1}^{r} \frac{\partial g_k}{\partial \epsilon_b}\Delta\epsilon_b + \sum_{c=1}^{m} \frac{\partial g_k}{\partial u_c}\Delta u_c. \tag{2.12}$$

Equations 2.10, 2.11, and 2.12 can be used to linearize non-linear dynamic systems.

Chapter 3

Internal Model Control (IMC)

Both Part II and Part III of this thesis deal with controllers based on the internal model principle. Therefore, the following sections provide insights into the concept of internal model control.

3.1 Introduction

Internal model control (IMC) is an alternative to conventional feedback control and has a long history in the process industry. In fact, IMC is a popular control method in chemical and mechanical engineering; however, its employment in the field of electrical power systems is a relatively new trend [1]. IMC is utilized in load frequency control [18, 19], the control of DC/DC converters [20], permanent magnet synchronous machines (PMSM) [21,22], and induction machine applications [23–25].

IMC is based on the internal model principle, which states that: *Control can be achieved only if the control system encapsulates, either implicitly or explicitly, some representation of the process to be controlled* [26].

Internal model control utilizes special PID controllers, occasionally augmented by a first-order lag, having only one tuning parameter (closed-loop time constant or bandwidth) as opposed to the three modes (k_c, τ_I, and τ_D) of ordinary PID controllers [27]. IMC combines the benefits of both the feedforward and feedback control methods. It is know for its simple design procedure making a trade-off between closed-loop performance and robustness against inaccuracies of the model [1, 27]. As its name implies, IMC's salient feature is the directly embedded model of the process to be controlled.

3.2 IMC Control Structure

Fig. 3.1 shows a block diagram of the internal model control method. The transfer functions $G_P(s)$, $\tilde{G}_P(s)$, and $G_C(s)$ represent the process, the model of the process, and the controller, respectively.

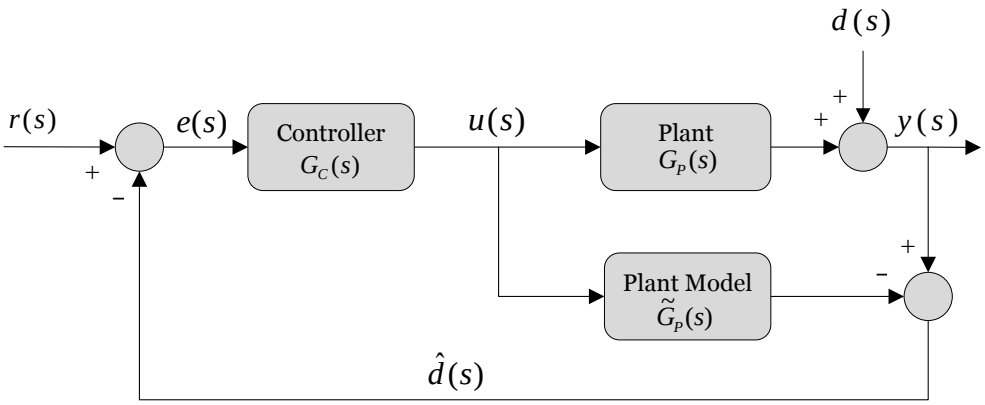

Figure 3.1: Block diagram of the internal model control (IMC) method [1].

Applying the control signal $u(s)$ to both the process $G_P(s)$ and its model $\tilde{G}_p(s)$ is distinctive of internal model control. Due to the parallel structure, the feedback signal $\tilde{d}(s)$ contains information about the disturbance $d(s)$ but also the mismatch between the process and its model (missing information). The feedback signal $\tilde{d}(s)$ is then deducted from the set point $r(s)$. The resulting error $e(s)$ is in turn applied to the controller $G_C(s)$ which generates the control signal $u(s)$. Salient is the feature that the error $e(s)$ is equal to the set point $r(s)$ in case of perfect tracking, while for the same scenario $e(s) = 0$ in standard feedback control [1].

However, the control structure shown in Fig. 3.1 is inappropriate for practical implementation. In order to rearrange it into the classical feedback form, the subtraction point leading to $\tilde{d}(s)$ is moved to the input of the controller $G_C(s)$ resulting in the block diagram shown in Fig. 3.2.

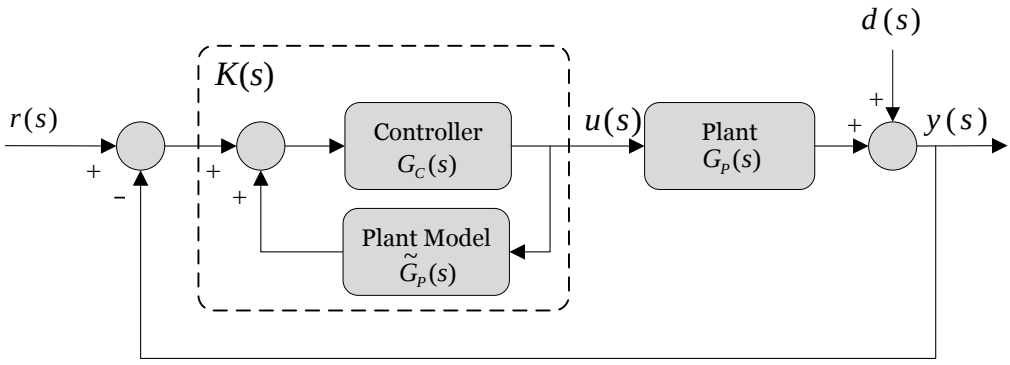

Figure 3.2: Block diagram of the internal model control (IMC) principle (classical feedback rearrangement) [1].

The equivalent standard feedback form of the IMC controller $K(s)$ is [1]:

$$K(s) = \frac{G_C(s)}{1 - G_C(s)\tilde{G}_P(s)}, \tag{3.1}$$

where $\tilde{G}_P(s)$ is the plant model and $G_C(s)$ is the inner controller. Ideally, $G_C(s)$ is chosen as the inverse of the plant model ($G_C(s) = \tilde{G}_P(s)^{-1}$). To make $G_C(s)$ proper, it is combined with a low-pass filter $G_{\text{LPF}}(s)$ of order n:

$$G_C(s) = \tilde{G}_P(s)^{-1} G_{\text{LPF}}(s) = \tilde{G}_P(s)^{-1} \frac{1}{(\lambda s + 1)^n}, \tag{3.2}$$

where λ is the tuning parameter.

The overall IMC-based controller $K(s)$ in Equation 3.1 then yields:

$$K(s) = \frac{\tilde{G}_P(s)^{-1}}{(\lambda s + 1)^n - 1}. \tag{3.3}$$

3.3 IMC Benefits

Reference [1] proposed a novel current controller for a voltage source converter based on internal model control. The authors ascertained that the IMC control approach, implemented in the *dq* reference frame, has superior control performance compared with conventional PI-based current control methods in the *dq* reference frame:

1. Faster step response;
2. Less overshoot in the transient response;

3. Higher axes decoupling; and
4. More robustness against faults.

Characteristics 1–3 are further investigated and elaborated in Part II and Part III of this thesis.

Part II

Small-Signal Stability Analysis of an Inverter-Based Microgrid with Internal Model–Based Controllers

The findings of Part II of this thesis have been submitted to *IEEE Transactions on Power Systems* as Leitner *et al.* [4].

Chapter 4

Introduction Part II

Due to an increase in environmental awareness in recent years, cut-backs on the use of fossil fuels and developments in the alternative energy sector have been accelerated. As a consequence, the electricity generation from renewable energy sources (RES), i.e., wind turbines, hydroelectric plants, photovoltaics, micro turbines, and fuel cells has increased significantly.

The integration of these mostly distributed generation (DG) units into the conventional power grid faces several challenges. As opposed to large central generating stations, control and management of a large number of small-scale DG units are difficult to accomplish [28–30].

Microgrids can help integrate DG units effectively and in turn improve the power grid's reliability and sustainability [6]. Many DG units utilize power electronic inverters, especially voltage source converters (VSC), to interface with the microgrid [31,32]. The key advantages of a power electronics–based interface are [33]:

- Improved power quality;
- Improved voltage regulation;
- Improved fault current coordination; and
- Reactive power (VAr) support.

On the downside, inverter-based microgrids are characterized by low inertia which causes challenges in maintaining stability and mitigating oscillations.

The use of PI-based controllers in zero-level control [11] dominates the control practice in inverter-based microgrids. PI-based controllers are extensively used and studied in the literature [10,11,34–37]. However, improving stability and transient

behavior of voltage and current is imperative for microgrids to allow more effective utilization of the assets and prevent violation of the operational limits [38, 39].

Recently, [1–3] proposed a cascade internal model control (IMC)–based voltage regulator consisting of an inner current controller and an outer voltage controller, as shown in Fig. 5.2. The authors perform time-domain simulations for a single DG unit and show that compared with PI-based controllers, the IMC-based approach has superior transient performance and is more robust against system parameter uncertainties. However, these studies are limited to a single DG unit and no systematic stability analysis is performed. In fact, while small-signal models are widely used in the literature, especially for PI-based controllers [10, 40], small-signal models for IMC-based controllers have not been developed yet.

Part II of this thesis studies the small-signal stability and transient behavior of a microgrid which incorporates IMC-based current and voltage controllers, giving an insight into the characteristic behavior of IMC controllers. As the first step, the state-space models of the current and voltage controllers are developed. Then, the state-space model of a microgrid incorporating IMC-based controllers is developed following the procedure presented in [10]. Using this state-space model, a detailed small-signal stability analysis is performed for a study microgrid system with three DG units. The results are compared with those of the same microgrid but with cascade PI-based controllers utilized in [10]. Moreover, PSCAD simulation case studies on transient behavior of the microgrid are performed for both methods to confirm the results of small-signal analysis. This study shows that compared with PI-based controllers, the characteristic behavior of IMC-based controllers includes:

- Increased damping ratios and frequencies of sensitive eigenvalues;
- Higher robustness to parameter changes; and
- Faster step response and reduced over/undershoot in current and voltage transients.

These advantages agree with the transient behavior of a single DG unit obtained from time-domain simulation case studies in [2].

The rest of Part II is organized as follows. The small-signal analysis is performed in Chapter 5, where the state-space small-signal models of the IMC-based voltage and current controllers are derived and incorporated into the model of a generic microgrid, and eigenvalue and sensitivity analysis are conducted. Finally, Chapter 6 recapitulates Part II and draws conclusions.

Chapter 5

Small-Signal Stability and Sensitivity Analysis of Internal Model Control

The following sections deal with the state-space modeling of a microgrid and its analysis. The voltage and current controllers of DG units are discussed, modeled, and tuned in detail. The state-space model of a generic microgrid with all its components is developed. The model is then used to perform eigenvalue and sensitivity analysis. The results are backed up by time-domain simulation case studies.

5.1 Control Structure of a DG Unit

Generally, the voltage source converter (VSC) of a DG unit is connected to the microgrid via a filter (e.g., RLC filter) in order to mitigate current and voltage harmonics and thereby improving the quality of the injected power, see Fig. 5.1. The zero-level control of the VSC usually comprises an inner current control loop and an outer voltage control loop [41, 42].

When the microgrid is in the islanded operating mode, the current controller regulates the injected current through the filter inductor, while the voltage controller regulates the DG unit output voltage (capacitor voltage). Hence, as can be seen in Fig. 5.1, the control of the DG unit is based on local measurements.

Although there exist different control approaches, PI-based voltage and current controllers dominate this application [10, 11, 34–37]. Assuming a balanced system with sinusoidal voltage and current waveforms, a rotating reference frame (RRF) is usually used to regulate the DG unit quantities in the direct and quadrature axes (d and q axes). As pointed out in Section 2.1, utilizing a RRF, independent control of

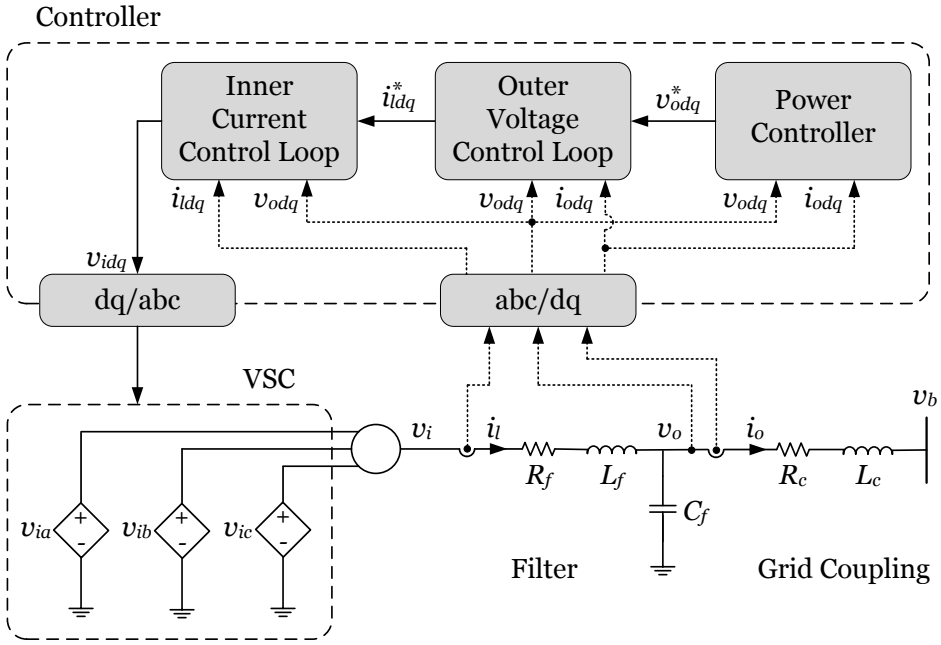

Figure 5.1: DG unit block diagram including controllers, VSC, filter, and grid connection.

grid-injected real and reactive power is facilitated.

As can be seen in Figs. 5.1, 5.2, and 5.3, depending on the DG unit output power to be delivered, the power controller provides the reference set-points (v^*_{od} and v^*_{oq}) for the outer voltage controller which in turn delivers the reference set-points (i^*_{ld} and i^*_{lq}) for the inner current controller. The output of the current controller (v_{id} and v_{iq}) then determines the gating signals of the VSC. In Part II of this thesis, for the sake of simplicity, the VSC is approximated with controlled voltage sources.

5.2 IMC-based Current and Voltage Controllers

Reference [2] recently proposed a novel cascade current and voltage control structure based on the internal model principle in the rotating dq reference frame shown in Fig. 5.2. The transfer functions of the outer voltage control loop $K_v(s)$ and $K'_v(s)$ are PD and PI controllers and the transfer functions of the inner current control loop $K_c(s)$ and $K'_c(s)$ are PID and PI controllers. The tuning of the IMC-based voltage and current controllers is shown in Section 5.3.

In the following subsections, the state-space small-signal models for the IMC-

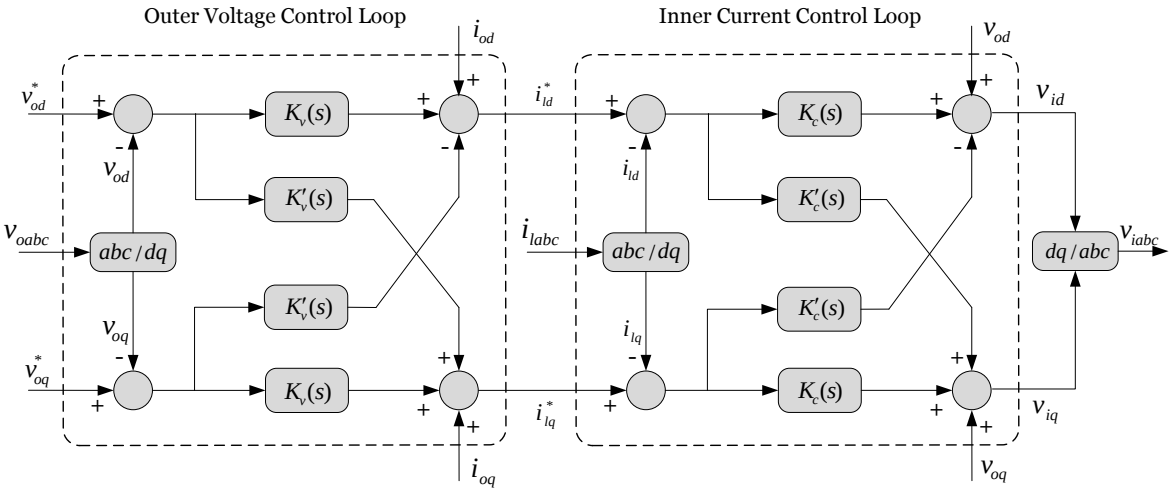

Figure 5.2: Block diagram of the IMC-based cascade voltage and current controllers of a VSC in the rotating dq reference frame [2].

based voltage and current controllers illustrated in Fig. 5.2 are derived. Generally, the integrator outputs are selected as state variables, which in turn makes their inputs derivatives of the state variables. Hence, the state equations of the inner current control loop, in direct and quadrature axes, are

$$\frac{d\gamma_d}{dt} = i^*_{ld} - i_{ld} \tag{5.1}$$

$$\frac{d\gamma_q}{dt} = i^*_{lq} - i_{lq}, \tag{5.2}$$

and those of the outer voltage control loop are

$$\frac{d\phi_d}{dt} = v^*_{od} - v_{od} \tag{5.3}$$

$$\frac{d\phi_q}{dt} = v^*_{oq} - v_{oq}, \tag{5.4}$$

where γ_d, γ_q, ϕ_d, and ϕ_q are the respective state variables. For brevity, time functions are stated without (t). The definition of all voltages and currents are based on Fig. 5.1. Subscripts d and q represent direct and quadrature axes, respectively, and $*$ refers to the reference value of a variable. Throughout Part II of this thesis, d- and q-components of the input vectors, output vectors, and state variables of the state-space small-signal models are aggregated as $\Delta z_{dq} = [\Delta z_d \ \Delta z_q]^T$.

5.2.1 IMC-Based Current Controller

This subsection derives the small-signal model of the inner current control loop shown in Fig. 5.2. In [2], the transfer functions $K_c(s)$ and $K'_c(s)$ are PID and PI controllers, respectively, with the tuning parameters K_{Pc}, K_{Ic}, K_{Dc}, K'_{Pc}, and K'_{Ic}. However, since a state-space representation requires proper transfer functions, the derivative terms of controllers are neglected, which is justifiable in this study as K_{Pc} and K_{Ic} are four and six orders of magnitude greater than K_{Dc}, see Section 5.3. From Fig. 5.2, the output equations of the inner current control loop are

$$v_{id}(s) = v_{od}(s) + \underbrace{\left[K_{Pc} + \frac{K_{Ic}}{s}\right]}_{K_c(s)}\left[i^*_{ld}(s) - i_{ld}(s)\right] - \underbrace{\left[K'_{Pc} + \frac{K'_{Ic}}{s}\right]}_{K'_c(s)}\left[i^*_{lq}(s) - i_{lq}(s)\right] \tag{5.5}$$

$$v_{iq}(s) = v_{oq}(s) + \underbrace{\left[K_{Pc} + \frac{K_{Ic}}{s}\right]}_{K_c(s)}\left[i^*_{lq}(s) - i_{lq}(s)\right] + \underbrace{\left[K'_{Pc} + \frac{K'_{Ic}}{s}\right]}_{K'_c(s)}\left[i^*_{ld}(s) - i_{ld}(s)\right]. \tag{5.6}$$

Applying inverse Laplace transform to Equations 5.5 and 5.6 and taking Equations 5.1 and 5.2 into account yields

$$v_{id} = v_{od} + K_{Pc}i^*_{ld} - K_{Pc}i_{ld} + K_{Ic}\gamma_d - K'_{Pc}i^*_{iq} + K'_{Pc}i_{lq} - K'_{Ic}\gamma_q \tag{5.7}$$

$$v_{iq} = v_{oq} + K_{Pc}i^*_{lq} - K_{Pc}i_{lq} + K_{Ic}\gamma_q + K'_{Pc}i^*_{ld} - K'_{Pc}i_{ld} + K'_{Ic}\gamma_d. \tag{5.8}$$

By linearizing and combining Equations 5.1, 5.2, 5.7, and 5.8, the small-signal model of the inner current control loop in state-space form is obtained as

$$\left[\Delta\dot{\gamma}_{dq}\right] = \underbrace{\begin{bmatrix}0 & 0\\ 0 & 0\end{bmatrix}}_{A_I}\left[\Delta\gamma_{dq}\right] + \underbrace{\begin{bmatrix}1 & 0\\ 0 & 1\end{bmatrix}}_{B_{I1}}\left[\Delta i^*_{ldq}\right] + \underbrace{\begin{bmatrix}-1 & 0 & 0 & 0 & 0 & 0\\ 0 & -1 & 0 & 0 & 0 & 0\end{bmatrix}}_{B_{I2}}\begin{bmatrix}\Delta i_{ldq}\\ \Delta v_{odq}\\ \Delta i_{odq}\end{bmatrix} \tag{5.9}$$

$$\left[\Delta v_{idq}\right] = \underbrace{\begin{bmatrix}K_{Ic} & -K'_{Ic}\\ K'_{Ic} & K_{Ic}\end{bmatrix}}_{C_I}\left[\Delta\gamma_{dq}\right] + \underbrace{\begin{bmatrix}K_{Pc} & -K'_{Pc}\\ K'_{Pc} & K_{Pc}\end{bmatrix}}_{D_{I1}}\left[\Delta i^*_{ldq}\right] + \underbrace{\begin{bmatrix}-K_{Pc} & K'_{Pc} & 1 & 0 & 0 & 0\\ -K'_{Pc} & -K_{Pc} & 0 & 1 & 0 & 0\end{bmatrix}}_{D_{I2}}\begin{bmatrix}\Delta i_{ldq}\\ \Delta v_{odq}\\ \Delta i_{odq}\end{bmatrix}.$$

(5.10)

The calculation of the control parameters K_{Pc}, K_{Ic}, K'_{Pc}, and K'_{Ic} is presented in Section 5.3. The values are also listed in Table 5.1.

Finally, Equations 5.11 and 5.12 represent the linearized small-signal state-space model of the IMC-based current controller as a linear time-invariant (LTI) system:

$$\underbrace{\begin{bmatrix}\Delta\dot{\gamma}_d\\ \Delta\dot{\gamma}_q\end{bmatrix}}_{\dot{X_I}(t)} = A_I \underbrace{\begin{bmatrix}\Delta\gamma_d\\ \Delta\gamma_q\end{bmatrix}}_{X_I(t)} + B_{I1} \underbrace{\begin{bmatrix}\Delta i^*_{ld}\\ \Delta i^*_{lq}\end{bmatrix}}_{U_{I1}(t)} + B_{I2} \underbrace{\begin{bmatrix}\Delta i_{ld}\\ \Delta i_{lq}\\ \Delta v_{od}\\ \Delta v_{oq}\\ \Delta i_{od}\\ \Delta i_{oq}\end{bmatrix}}_{U_{I2}(t)} \tag{5.11}$$

$$\underbrace{\begin{bmatrix}\Delta v_{id}\\ \Delta v_{iq}\end{bmatrix}}_{Y_I(t)} = C_I \underbrace{\begin{bmatrix}\Delta\gamma_d\\ \Delta\gamma_q\end{bmatrix}}_{X_I(t)} + D_{I1} \underbrace{\begin{bmatrix}\Delta i^*_{ld}\\ \Delta i^*_{lq}\end{bmatrix}}_{U_{I1}(t)} + D_{I2} \underbrace{\begin{bmatrix}\Delta i_{ld}\\ \Delta i_{lq}\\ \Delta v_{od}\\ \Delta v_{oq}\\ \Delta i_{od}\\ \Delta i_{oq}\end{bmatrix}}_{U_{I2}(t)}, \tag{5.12}$$

where the vector $X_I(t)$ represents the states, vectors $U_{I1}(t)$ and $U_{I2}(t)$ represent the input quantities, and vector $Y_I(t)$ represents the output quantities of the current controller.

5.2.2 IMC-Based Voltage Controller

This subsection derives the small-signal model of the outer voltage control loop depicted in Fig. 5.2. In [2], the transfer functions $K_v(s)$ and $K'_v(s)$ are PD and PI controllers, respectively, with the tuning parameters K_{Pv}, K_{Dv}, K'_{Pv}, and K'_{Iv}. The derivative terms are omitted since a state-space representation needs proper transfer functions, which is justifiable in this study because K_{Dv} is 500 times smaller than K_{Pv}, see Section 5.3. The output equations of the outer voltage control loop can be derived

from Fig. 5.2 as follows:

$$i_{ld}^{*}(s) = i_{od}(s) + \underbrace{K_{Pv}}_{K_v(s)}\left[v_{od}^{*}(s) - v_{od}(s)\right] - \underbrace{\left[K'_{Pv} + \frac{K'_{Iv}}{s}\right]}_{K'_v(s)}\left[v_{oq}^{*}(s) - v_{oq}(s)\right] \tag{5.13}$$

$$i_{lq}^{*}(s) = i_{oq}(s) + \underbrace{K_{Pv}}_{K_v(s)}\left[v_{oq}^{*}(s) - v_{oq}(s)\right] + \underbrace{\left[K'_{Pv} + \frac{K'_{Iv}}{s}\right]}_{K'_v(s)}\left[v_{od}^{*}(s) - v_{od}(s)\right]. \tag{5.14}$$

Applying inverse Laplace transform to Equations 5.13 and 5.14, and taking Equations 5.3 and 5.4 into account, the following algebraic equations for the outer voltage control loop can be derived:

$$i_{ld}^{*} = i_{od} + K_{Pv}v_{od}^{*} - K_{Pv}v_{od} - K'_{Pv}v_{oq}^{*} + K'_{Pv}v_{oq} - K'_{Iv}\phi_q \tag{5.15}$$

$$i_{lq}^{*} = i_{oq} + K_{Pv}v_{oq}^{*} - K_{Pv}v_{oq} + K'_{Pv}v_{od}^{*} - K'_{Pv}v_{od} + K'_{Iv}\phi_d. \tag{5.16}$$

By linearizing and combining Equations 5.3, 5.4, 5.15, and 5.16, the small-signal model of the outer voltage control loop in state-space form can be written as follows:

$$\left[\Delta\dot{\phi}_{dq}\right] = \underbrace{\begin{bmatrix}0 & 0\\ 0 & 0\end{bmatrix}}_{A_V}\left[\Delta\phi_{dq}\right] + \underbrace{\begin{bmatrix}1 & 0\\ 0 & 1\end{bmatrix}}_{B_{V1}}\left[\Delta v_{odq}^{*}\right] + \underbrace{\begin{bmatrix}0 & 0 & -1 & 0 & 0 & 0\\ 0 & 0 & 0 & -1 & 0 & 0\end{bmatrix}}_{B_{V2}}\begin{bmatrix}\Delta i_{ldq}\\ \Delta v_{odq}\\ \Delta i_{odq}\end{bmatrix} \tag{5.17}$$

$$\left[\Delta i_{ldq}^{*}\right] = \underbrace{\begin{bmatrix}0 & -K'_{Iv}\\ K'_{Iv} & 0\end{bmatrix}}_{C_V}\left[\Delta\phi_{dq}\right] + \underbrace{\begin{bmatrix}K_{Pv} & -K'_{Pv}\\ K'_{Pv} & K_{Pv}\end{bmatrix}}_{D_{V1}}\left[\Delta v_{odq}^{*}\right] + \underbrace{\begin{bmatrix}0 & 0 & -K_{Pv} & K'_{Pv} & 1 & 0\\ 0 & 0 & -K'_{Pv} & -K_{Pv} & 0 & 1\end{bmatrix}}_{D_{V2}}\begin{bmatrix}\Delta i_{ldq}\\ \Delta v_{odq}\\ \Delta i_{odq}\end{bmatrix}. \tag{5.18}$$

The calculation of the control parameters K_{Pv}, K'_{Pv}, and K'_{Iv} is presented in Section 5.3. The values are also listed in Table 5.1.

Finally, Equations 5.19 and 5.20 represent the linearized small-signal state-space model of the IMC-based outer voltage controller as a linear time-invariant (LTI) system:

$$\underbrace{\begin{bmatrix}\Delta\dot{\phi}_d\\ \Delta\dot{\phi}_q\end{bmatrix}}_{\dot{X_V}(t)} = A_V \underbrace{\begin{bmatrix}\Delta\phi_d\\ \Delta\phi_q\end{bmatrix}}_{X_V(t)} + B_{V1} \underbrace{\begin{bmatrix}\Delta v^*_{od}\\ \Delta v^*_{oq}\end{bmatrix}}_{U_{V1}(t)} + B_{V2} \underbrace{\begin{bmatrix}\Delta i_{ld}\\ \Delta i_{lq}\\ \Delta v_{od}\\ \Delta v_{oq}\\ \Delta i_{od}\\ \Delta i_{oq}\end{bmatrix}}_{U_{V2}(t)} \tag{5.19}$$

$$\underbrace{\begin{bmatrix}\Delta i^*_{ld}\\ \Delta i^*_{lq}\end{bmatrix}}_{Y_V(t)} = C_V \underbrace{\begin{bmatrix}\Delta\phi_d\\ \Delta\phi_q\end{bmatrix}}_{X_V(t)} + D_{V1} \underbrace{\begin{bmatrix}\Delta v^*_{od}\\ \Delta v^*_{oq}\end{bmatrix}}_{U_{V1}(t)} + D_{V2} \underbrace{\begin{bmatrix}\Delta i_{ld}\\ \Delta i_{lq}\\ \Delta v_{od}\\ \Delta v_{oq}\\ \Delta i_{od}\\ \Delta i_{oq}\end{bmatrix}}_{U_{V2}(t)}, \tag{5.20}$$

where the vector $X_V(t)$ represents the states, vectors $U_{V1}(t)$ and $U_{V2}(t)$ represent the input quantities, and vector $Y_V(t)$ represents the output quantities of the voltage controller.

5.3 Tuning the Control Parameters

In this section, the control parameters of the IMC-based inner current and outer voltage controllers are determined based on [1,3].

5.3.1 Inner Current Controller

The transfer functions of the IMC-based inner current controller in Fig. 5.2 utilizing PID and PI controllers are:

$$K_c(s) = \frac{k_d s^2 + k_p s + k_i}{s} \tag{5.21}$$

$$K_c'(s) = \frac{k_p' s + k_i'}{s}. \tag{5.22}$$

The control parameters of the current controller are calculated based on the used RL filter of the DG unit and are tuned with the only tuning parameter λ_c. The VSC is modeled as a time delay (digitalization and PWM transport delay) which is assumed as $T_{\text{PWM}} = 1/(2f_{\text{sw}}) = 1/(2 \times 8000\text{Hz}) = 6.25 \times 10^{-5}$ s. With a tuning parameter of $\lambda_c = 10^{-5}$, the control parameters of the current controller result in:

$$\begin{cases} k_p = K_{Pc} = \frac{R_f T_{\text{PWM}} + L_f}{\lambda_c} = \frac{0.1\Omega \times 6.25\times10^{-5}\text{s} + 1.35\text{mH}}{10^{-5}} = 135.625 \\ k_i = K_{Ic} = \frac{R_f + T_{\text{PWM}} L_f \omega^2}{\lambda_c} = \frac{0.1\Omega + 6.25\times10^{-5}\text{s}\times 1.35\text{mH}\times(2\pi 50\text{Hz})^2}{10^{-5}} = 9.1673 \times 10^3 \\ k_d = K_{Dc} = \frac{T_{\text{PWM}} L_f}{\lambda_c} = \frac{6.25\times10^{-5}\text{s}\times 1.35\text{mH}}{10^{-5}} = 0.0084 \end{cases} \tag{5.23}$$

and

$$\begin{cases} k_p' = K_{Pc}' = \frac{2\omega L_f T_{\text{PWM}}}{\lambda_c} = \frac{2\times 2\pi 50\text{Hz}\times 1.35\text{mH}\times 6.25\times10^{-5}\text{s}}{10^{-5}} = 5.3014 \\ k_i' = K_{Ic}' = \frac{2(L_f + R_f T_{\text{PWM}})}{\lambda_c} = \frac{2(1.35\text{mH} + 0.1\Omega\times 6.25\times10^{-5}\text{s})}{10^{-5}} = 4.2608 \times 10^4. \end{cases} \tag{5.24}$$

The control parameters of the IMC-based current controller are also listed in Table 5.1.

5.3.2 Outer Voltage Controller

The transfer functions of the IMC-based outer voltage controller in Fig. 5.2 utilizing PD and PI controllers are:

$$K_v(s) = \frac{k_d s^2 + k_p s}{s} \tag{5.25}$$

$$K_v'(s) = \frac{k_p' s + k_i'}{s}. \tag{5.26}$$

The control parameters of the voltage controller are calculated based on the used C filter of the DG unit and are tuned with the only tuning parameter λ_v. Since the outer voltage controller delivers the set points for the inner current controller, the time delay of the current control loop (including VSC delay) needs to be taken into account and is assumed as $T_c = 2$ ms. With a tuning parameter of $\lambda_v = 2 \times 10^{-4}$, the control parameters of the current controller result in:

$$\begin{cases} k_p = K_{Pv} = \frac{C_f}{\lambda_v} = \frac{50\mu\text{F}}{2\times10^{-4}} = 0.25 \\ k_d = K_{Dv} = \frac{C_f T_c}{\lambda_v} = \frac{50\mu F\times 2\text{ms}}{2\times10^{-4}} = 5 \times 10^{-4} \end{cases} \tag{5.27}$$

and

$$\begin{cases} k'_p = K'_{Pv} = \frac{C_f \omega T_c}{\lambda_v} = \frac{50\mu F \times 2\pi 50\text{Hz} \times 2\text{ms}}{2\times 10^{-4}} = 0.1571 \\ k'_i = K'_{Iv} = \frac{2C_f \omega}{\lambda_v} = \frac{2\times 50\mu F \times 2\pi 50\text{Hz}}{2\times 10^{-4}} = 78.5398. \end{cases} \tag{5.28}$$

The control parameters of the IMC-based voltage controller are also listed in Table 5.1.

5.4 Conventional PI-based Current and Voltage Controllers

Fig. 5.3 shows the control structure of the conventional PI-based cascade current and voltage controllers, where $K_c(s)$ and $K_v(s)$ are PI-based current and voltage controllers in the d and q axes and ωC and ωL are the cross-coupling terms aiming to improve the transient behavior.

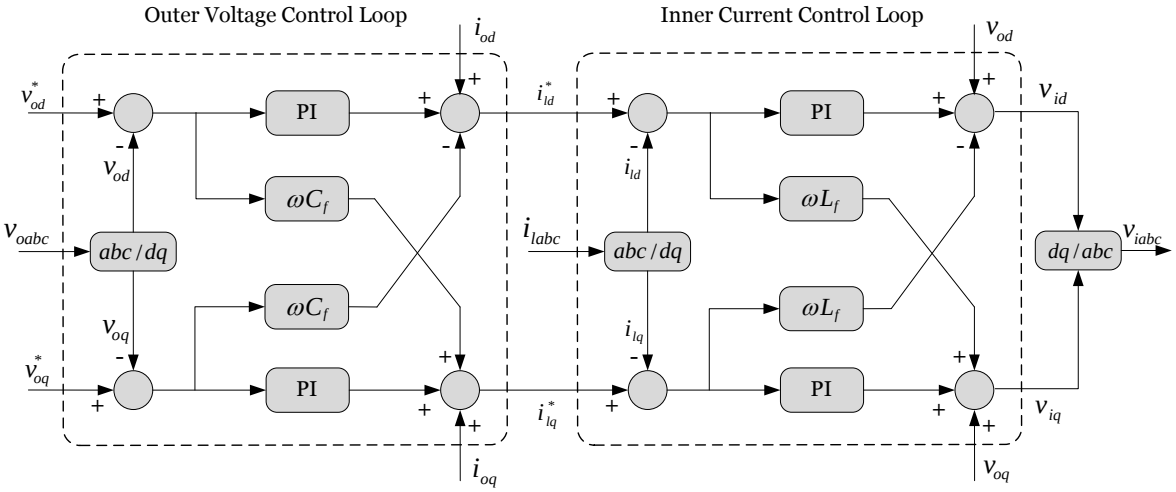

Figure 5.3: Block diagram of the conventional PI-based cascade voltage and current controllers of a VSC in the rotating dq reference frame [3].

Using the procedure from Subsection 5.2.1, the state-space small-signal model of the conventional PI-based inner current control loop in Fig. 5.3 can be derived as [10]:

$$\left[\Delta\dot{\gamma}_{dq}\right] = \underbrace{\begin{bmatrix} 0 & 0 \\ 0 & 0 \end{bmatrix}}_{A_C} \left[\Delta\gamma_{dq}\right] + \underbrace{\begin{bmatrix} 1 & 0 \\ 0 & 1 \end{bmatrix}}_{B_{C1}} \left[\Delta i^*_{ldq}\right] + \underbrace{\begin{bmatrix} -1 & 0 & 0 & 0 & 0 & 0 \\ 0 & -1 & 0 & 0 & 0 & 0 \end{bmatrix}}_{B_{C2}} \begin{bmatrix} \Delta i_{ldq} \\ \Delta v_{odq} \\ \Delta i_{odq} \end{bmatrix} \tag{5.29}$$

$$\left[\Delta v_{idq}\right] = \underbrace{\begin{bmatrix} K_{Ic} & 0 \\ 0 & K_{Ic} \end{bmatrix}}_{C_C}\left[\Delta \gamma_{dq}\right] + \underbrace{\begin{bmatrix} K_{Pc} & 0 \\ 0 & K_{Pc} \end{bmatrix}}_{D_{C1}}\left[\Delta i^*_{ldq}\right] + \underbrace{\begin{bmatrix} -K_{Pc} & -\omega_n L_f & 0 & 0 & 0 & 0 \\ \omega_n L_f & -K_{Pc} & 0 & 0 & 0 & 0 \end{bmatrix}}_{D_{C2}}\begin{bmatrix} \Delta i_{ldq} \\ \Delta v_{odq} \\ \Delta i_{odq} \end{bmatrix}. \tag{5.30}$$

Similarly, using the procedure from Subsection 5.2.2, the state-space small-signal model of the PI-based outer voltage control loop can be derived as [10]:

$$\left[\Delta \dot{\phi}_{dq}\right] = \underbrace{\begin{bmatrix} 0 & 0 \\ 0 & 0 \end{bmatrix}}_{A_V}\left[\Delta \phi_{dq}\right] + \underbrace{\begin{bmatrix} 1 & 0 \\ 0 & 1 \end{bmatrix}}_{B_{V1}}\left[\Delta v^*_{odq}\right] + \underbrace{\begin{bmatrix} 0 & 0 & -1 & 0 & 0 & 0 \\ 0 & 0 & 0 & -1 & 0 & 0 \end{bmatrix}}_{B_{V2}}\begin{bmatrix} \Delta i_{ldq} \\ \Delta v_{odq} \\ \Delta i_{odq} \end{bmatrix} \tag{5.31}$$

$$\left[\Delta i^*_{ldq}\right] = \underbrace{\begin{bmatrix} K_{Iv} & 0 \\ 0 & K_{Iv} \end{bmatrix}}_{C_V}\left[\Delta \phi_{dq}\right] + \underbrace{\begin{bmatrix} K_{Pv} & 0 \\ 0 & K_{Pv} \end{bmatrix}}_{D_{V1}}\left[\Delta v^*_{odq}\right] + \underbrace{\begin{bmatrix} 0 & 0 & -K_{Pv} & -\omega_n C_f & F & 0 \\ 0 & 0 & \omega_n C_f & -K_{Pv} & 0 & F \end{bmatrix}}_{D_{V2}}\begin{bmatrix} \Delta i_{ldq} \\ \Delta v_{odq} \\ \Delta i_{odq} \end{bmatrix}. \tag{5.32}$$

The control parameters used in this paper for the conventional PI-based method (K_{Pc}, K_{Ic}, K_{Pv}, and K_{Iv}) are the same as those reported in [10].

5.5 State-Space Model of a Generic Microgrid

This section discusses the small-signal model of a microgrid study system that includes power controllers, filters, inverters, lines, and loads based on [10]. It is shown how the previously derived IMC-based current and voltage controllers are combined with the submodels of the power controllers, filters, inverters, lines, and loads to form the linearized system matrix A_{MG}. The notation diag() is used to show the nonzero elements of a diagonal matrix.

5.5.1 Power Controller Model

This subsection focuses on the power controller block in Fig. 5.1. In this study, power controllers utilizing conventional droop control (see Fig. 5.4) are employed to share

real and reactive power between inverters in the microgrid shown in Fig. 5.5.

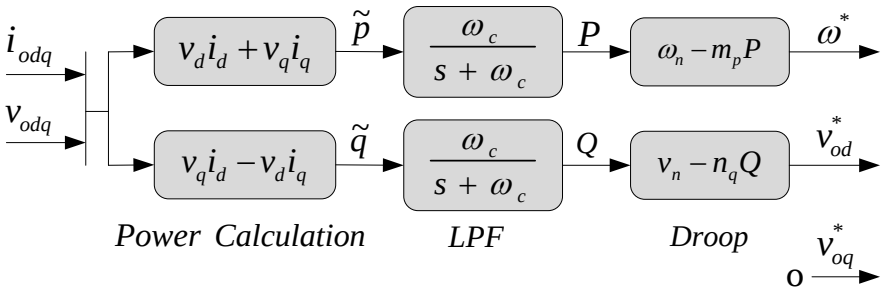

Figure 5.4: Block diagram of the power controller [4].

As derived in Section 2.1, the instantaneous power $\tilde{s}$ in the dq-frame can be calculated as follows:

$$\tilde{s} = \underbrace{(v_d i_d + v_q i_q)}_{\tilde{p}} + j\underbrace{(v_q i_d - v_d i_q)}_{\tilde{q}}, \tag{5.33}$$

where $\tilde{p}$, and $\tilde{q}$ are the instantaneous real and reactive power components of the instantaneous power $\tilde{s}$; and v_d, v_q, i_d, and i_q are the dq-components of the output voltage and current of the DG unit (v_o and i_o in Fig. 5.1).

The instantaneous real and reactive power components are then passed through a low-pass filter (LPF) with the cut-off frequency ω_c to yield the average real and reactive power values P and Q which are in turn used in the droop equations.

As can be seen in Fig. 5.4, in conventional droop control, an increase in the real output power artificially reduces the reference value of the inverter frequency ω^*. Similarly, an increase in the reactive output power reduces the reference output voltage v_{od}^* of the inverter while v_{oq}^* is set to zero. The equations of the conventional droop control are:

$$\omega^* = \omega_n - m_p P \tag{5.34}$$

$$v_{od}^* = v_{odn} - n_q Q, \tag{5.35}$$

where ω_n and v_{odn} are the nominal values of the inverter angular frequency and the output voltage d-component. The coefficients m_p and n_q are the real and reactive power droop gains which depend on the DG unit capacity (Pmax, Qmin, Qmax) and

grid code (fmin, Vmax, Vmin) [43]. With Equation 5.34, the inverter angle in the rotating dq reference frame can be determined as

$$\delta = \int (\omega^* - \omega_{\text{com}}) dt, \tag{5.36}$$

where ω_{com} represents the angular speed of the reference inverter (side note: the angle of the reference inverter is 0 as $\omega^* = \omega_{\text{com}}$ in that case).

Deriving Equation 5.36 with respect to time yields the linearized state equation of the respective inverter angle:

$$\Delta\dot{\delta} = -m_p \Delta P - \Delta\omega_{\text{com}}. \tag{5.37}$$

Similarly, taking the power calculation in Equation 5.33 into account and applying the procedure presented in Section 2.2 to Equations 5.34 and 5.35 yields with Equation 5.37 the small-signal state-space model of the power controller utilizing conventional droop control:

$$\begin{bmatrix} \Delta\dot{\delta} \\ \Delta\dot{P} \\ \Delta\dot{Q} \end{bmatrix} = \underbrace{\begin{bmatrix} 0 & -m_p & 0 \\ 0 & -\omega_c & 0 \\ 0 & 0 & -\omega_c \end{bmatrix}}_{A_P} \begin{bmatrix} \Delta\delta \\ \Delta P \\ \Delta Q \end{bmatrix} + \underbrace{\begin{bmatrix} -1 \\ 0 \\ 0 \end{bmatrix}}_{B_{P\omega\text{com}}} \Delta\omega_{\text{com}} + \underbrace{\begin{bmatrix} 0 & 0 & 0 & 0 & 0 & 0 \\ 0 & 0 & \omega_c I_{od} & \omega_c I_{oq} & \omega_c V_{od} & \omega_c V_{oq} \\ 0 & 0 & -\omega_c I_{oq} & \omega_c I_{od} & \omega_c V_{oq} & -\omega_c V_{od} \end{bmatrix}}_{B_P} \begin{bmatrix} \Delta i_{ldq} \\ \Delta v_{odq} \\ \Delta i_{odq} \end{bmatrix} \tag{5.38}$$

$$\begin{bmatrix} \Delta\omega^* \\ \Delta v_{od}^* \\ \Delta v_{oq}^* \end{bmatrix} = \underbrace{\begin{bmatrix} 0 & -m_p & 0 \\ 0 & 0 & -n_q \\ 0 & 0 & 0 \end{bmatrix}}_{C_P} \begin{bmatrix} \Delta\delta \\ \Delta P \\ \Delta Q \end{bmatrix} \tag{5.39}$$

$$C_P = \left[\begin{array}{c} [C_{P\omega}]_{1\times 3} \\ \hdashline [C_{Pv}]_{2\times 3} \end{array} \right]_{3\times 3}. \tag{5.40}$$

The quantities I_{od}, I_{oq}, V_{od}, and V_{oq} are steady state values taken from [10] and represent the operating state in whose neighborhood the linearization takes place.

5.5.2 Filter and Grid Connection Model

Due to switching, output currents and voltages of power electronic converters (e.g., VSCs) are significantly distorted and contain harmonics. In this study, a low-pass filter plus grid coupling inductor provide a remedy (see Fig. 5.1). The linearized small-signal state-space model of the output LC filter and grid coupling inductance L_c (including equivalent series resistors R_f and R_c) is as follows [10]:

$$\begin{bmatrix} \Delta\dot{i}_{ldq} \\ \Delta\dot{v}_{odq} \\ \Delta\dot{i}_{odq} \end{bmatrix} = A_{\mathrm{LCL}} \begin{bmatrix} \Delta i_{ldq} \\ \Delta v_{odq} \\ \Delta i_{odq} \end{bmatrix} + B_{\mathrm{LCL1}}[\Delta v_{idq}] + B_{\mathrm{LCL2}}[\Delta v_{bdq}] + B_{\mathrm{LCL3}}[\Delta\omega], \tag{5.41}$$

where

$$A_{\mathrm{LCL}} = \begin{bmatrix} \frac{-R_f}{L_f} & \omega_0 & \frac{-1}{L_f} & 0 & 0 & 0 \\ -\omega_0 & \frac{-R_f}{L_f} & 0 & \frac{-1}{L_f} & 0 & 0 \\ \frac{1}{C_f} & 0 & 0 & \omega_0 & \frac{-1}{C_f} & 0 \\ 0 & \frac{1}{C_f} & -\omega_0 & 0 & 0 & \frac{-1}{C_f} \\ 0 & 0 & \frac{1}{L_c} & 0 & \frac{-R_c}{L_c} & \omega_0 \\ 0 & 0 & 0 & \frac{1}{L_c} & -\omega_0 & \frac{-R_c}{L_c} \end{bmatrix} \tag{5.42}$$

$$B_{\mathrm{LCL1}} = \begin{bmatrix} \frac{1}{L_f} & 0 \\ 0 & \frac{1}{L_f} \\ 0 & 0 \\ 0 & 0 \\ 0 & 0 \\ 0 & 0 \end{bmatrix} \tag{5.43}$$

$$B_{\mathrm{LCL2}} = \begin{bmatrix} 0 & 0 \\ 0 & 0 \\ 0 & 0 \\ 0 & 0 \\ \frac{-1}{L_c} & 0 \\ 0 & \frac{-1}{L_c} \end{bmatrix} \tag{5.44}$$

$$B_{\mathrm{LCL3}} = \begin{bmatrix} I_{lq} & -I_{ld} & V_{oq} & -V_{od} & I_{oq} & -I_{od} \end{bmatrix}^T. \tag{5.45}$$

The quantities are defined in Fig. 5.1 and the system parameters in the above matrices are listed in Table 5.1.

5.5.3 Transformation of Inverter Parameters

In this study, a rotating reference frame (RRF) is utilized to describe the voltages and currents in the microgrid. Generally, one of the inverters is chosen to be the reference inverter while the lines, loads, and other inverters are translated into the so called common reference frame. T_{Si} is used to transform the dq-components of inverter i into the DQ reference frame [44], rotating at a speed of ω_{com}:

$$[f_{DGi}] = \underbrace{\begin{bmatrix} \cos(\delta_i) & -\sin(\delta_i) \\ \sin(\delta_i) & \cos(\delta_i) \end{bmatrix}}_{T_{Si}} [f_{dqi}], \tag{5.46}$$

where δ_i is the angle of inverter i.

The output variable of the inverter i is its output current, which can be transformed into the RRF, resulting in the output current $[\Delta i_{oDQi}]$, as

$$[\Delta i_{oDQi}] = T_{Si}[\Delta i_{odqi}] + T_{Ci}[\Delta\delta_i], \tag{5.47}$$

where

$$T_{Si} = \begin{bmatrix} \cos(\delta_{0i}) & -\sin(\delta_{0i}) \\ \sin(\delta_{0i}) & \cos(\delta_{0i}) \end{bmatrix}_{2\times 2}, \tag{5.48}$$

$$T_{Ci} = \begin{bmatrix} -I_{odi}\sin(\delta_{0i}) - I_{oqi}\cos(\delta_{0i}) \\ I_{odi}\cos(\delta_{0i}) - I_{oqi}\sin(\delta_{0i}) \end{bmatrix}_{2\times 1}, \tag{5.49}$$

and δ_{0i} is the steady state inverter angle (initial condition displacement).

The input variable of the inverter i is the bus voltage $[\Delta v_{bdqi}]$, which can be obtained from the bus voltages in the RRF $[\Delta v_{bDQi}]$ as follows:

$$[\Delta v_{bdqi}] = T_{Si}^{-1}[\Delta v_{bDQi}] + T_{Vi}^{-1}[\Delta\delta_i], \tag{5.50}$$

where

$$T_{Vi}^{-1} = \begin{bmatrix} -V_{bDi}\sin(\delta_{0i}) + V_{bQi}\cos(\delta_{0i}) \\ -V_{bDi}\cos(\delta_{0i}) - V_{bQi}\sin(\delta_{0i}) \end{bmatrix}_{2\times 1}. \tag{5.51}$$

5.5.4 Complete Model of Inverter i

In this subsection, the small-signal models of the derived current and voltage controllers, along with the power controller, filter, and grid coupling inductor combine to form the complete model of inverter i (model of the DG unit shown in Fig. 5.1):

$$[\Delta \dot{x}_{\mathrm{INV}i}] = A_{\mathrm{INV}i}[\Delta x_{\mathrm{INV}i}] + B_{\mathrm{INV}i}[\Delta v_{bDQi}] + B_{i\omega\mathrm{com}}\Delta\omega_{\mathrm{com}} \tag{5.52}$$

$$\begin{bmatrix} \Delta\omega_i \\ \Delta i_{oDQi} \end{bmatrix} = \begin{bmatrix} C_{\mathrm{INV}\omega i} \\ C_{\mathrm{INV}ci} \end{bmatrix} [\Delta x_{\mathrm{INV}i}], \tag{5.53}$$

where

$$[\Delta x_{\mathrm{INV}i}] = [\Delta\delta_i \ \Delta P_i \ \Delta Q_i \ \Delta\varphi_{dqi} \ \Delta\gamma_{dqi} \ \Delta i_{ldqi} \ \Delta v_{odqi} \ \Delta i_{odqi}]^T \tag{5.54}$$

$$B_{\mathrm{INV}i} = \left[\begin{array}{c} [\mathbf{0}]_{7\times2} \\ \hline B_{\mathrm{LCL2}i} T_{Si}^{-1} \end{array}\right]_{13\times2} \tag{5.55}$$

$$B_{i\omega\mathrm{com}} = \left[\begin{array}{c} B_{P\omega\mathrm{com}} \\ \hline [\mathbf{0}]_{10\times1} \end{array}\right]_{13\times1} \tag{5.56}$$

$$C_{\mathrm{INV}\omega i} = \begin{cases} [C_{P\omega} \ 0 \ \dots \ 0]_{1\times13} & i = 1 \\ [\mathbf{0}]_{1\times13} & i \neq 1 \end{cases} \tag{5.57}$$

$$C_{\mathrm{INV}ci} = \left[\begin{array}{c|c|c} T_{Ci} & [\mathbf{0}]_{2\times10} & T_{Si} \end{array}\right]_{2\times13} \tag{5.58}$$

$$A_{\mathrm{INV}i} = \left[\begin{array}{c|c|c|c} A_{Pi} & [\mathbf{0}]_{3\times2} & [\mathbf{0}]_{3\times2} & B_{Pi} \\ \hline B_{V1i}C_{Pvi} & [\mathbf{0}]_{2\times2} & [\mathbf{0}]_{2\times2} & B_{V2i} \\ \hline B_{V1i}D_{V1i}C_{Pvi} & B_{C1i}C_{Vi} & [\mathbf{0}]_{2\times2} & B_{C1i}D_{V2i} + B_{C2i} \\ \hline \begin{array}{l} B_{\mathrm{LCL1}i}D_{C1i}D_{V1i}C_{Pvi} \\ +B_{\mathrm{LCL2}i}\left[\begin{array}{c|c} T_{Vi}^{-1} & [\mathbf{0}]_{2\times2} \end{array}\right] \\ +B_{\mathrm{LCL3}i}C_{P\omega i} \end{array} & B_{\mathrm{LCL1}i}D_{C1i}C_{Vi} & B_{\mathrm{LCL1}i}C_{Ci} & \begin{array}{c} A_{\mathrm{LCL}i} \\ +B_{\mathrm{LCL1}i}[D_{C1i}D_{V2i} + D_{C2i}] \end{array} \end{array}\right]_{13\times13}. \tag{5.59}$$

5.5.5 Complete Model of all Inverters in the Microgrid

Using the previously derived small-signal model of inverter i, this subsection shows how these individual inverter models can be combined to form the generic small-signal model of k inverters in a microgrid with m nodes:

$$[\Delta\dot{x}_{\mathrm{INV}}] = A_{\mathrm{INV}}[\Delta x_{\mathrm{INV}}] + B_{\mathrm{INV}}[\Delta v_{bDQ}] \tag{5.60}$$

$$[\Delta\dot{i}_{oDQ}] = C_{\mathrm{INV}c}[\Delta x_{\mathrm{INV}}], \tag{5.61}$$

where

$$[\Delta x_{\text{INV}}] = [\Delta x_{\text{INV1}}\ \Delta x_{\text{INV2}}\ \ldots\ \Delta x_{\text{INV}k}]^T_{2k\times 1} \tag{5.62}$$

$$[\Delta v_{b\text{DG}}] = [\Delta v_{b\text{DG1}}\ \Delta v_{b\text{DG2}}\ \ldots\ \Delta v_{b\text{DG}n}]^T_{2k\times 1} \tag{5.63}$$

$$B_{\text{INV}} = \text{diag}([B_{\text{INV1}}, B_{\text{INV2}}, \ldots, B_{\text{INV}k}])_{13k\times 2m} \tag{5.64}$$

$$C_{\text{INV}c} = \text{diag}([C_{\text{INV}c1}, C_{\text{INV}c2}, \ldots, C_{\text{INV}ck}])_{2k\times 13k} \tag{5.65}$$

$$A_{\text{INV}} = \begin{bmatrix} A_{\text{INV1}} + B_{1\omega\text{com}}C_{\text{INV}\omega 1} & [\mathbf{0}]_{13\times 13} & [\mathbf{0}]_{13\times 13} & \cdots & [\mathbf{0}]_{13\times 13} \\ X_{m_p} & A_{\text{INV2}} + B_{2\omega\text{com}}C_{\text{INV}\omega 2} & [\mathbf{0}]_{13\times 13} & \cdots & [\mathbf{0}]_{13\times 13} \\ X_{m_p} & [\mathbf{0}]_{13\times 13} & \ddots & \ddots & \vdots \\ \vdots & \vdots & \ddots & \ddots & [\mathbf{0}]_{13\times 13} \\ X_{m_p} & [\mathbf{0}]_{13\times 13} & \cdots & [\mathbf{0}]_{13\times 13} & A_{\text{INV}k} + B_{k\omega\text{com}}C_{\text{INV}\omega k} \end{bmatrix}_{13k\times 13k} \tag{5.66}$$

$$X_{m_p} = \begin{bmatrix} 0 & m_p & 0 & \ldots & 0 \\ 0 & 0 & 0 & \ldots & 0 \\ \vdots & \vdots & \vdots & \ddots & \vdots \\ 0 & 0 & 0 & \ldots & 0 \end{bmatrix}_{13\times 13}, \tag{5.67}$$

where inverter 1 (entry $A_{\text{INV}}(1,1)$) is chosen to be the common reference frame. The m_p entry in Equation 5.67 influences the angles of the remaining inverters in the RRF and accounts for rotational speed changes of the reference inverter (inverter 1).

The studied microgrid has three DG units (see Fig. 5.5). Applying the derived generic small-signal inverter model to the study microgrid system having three inverters, the matrices B_{INV}, $C_{\text{INV}c}$, and A_{INV} in Equation 5.60 and 5.61 reduce to:

$$B_{\text{INV}} = \begin{bmatrix} B_{\text{INV1}} & [0]_{13\times 2} & [0]_{13\times 2} \\ [0]_{13\times 2} & B_{\text{INV2}} & [0]_{13\times 2} \\ [0]_{13\times 2} & [0]_{13\times 2} & B_{\text{INV3}} \end{bmatrix}_{39\times 6} \tag{5.68}$$

$$C_{\text{INVc}} = \left[\begin{array}{c|c|c} C_{\text{INVc1}} & [0]_{13\times2} & [0]_{13\times2} \\ \hline [0]_{13\times2} & C_{\text{INVc2}} & [0]_{13\times2} \\ \hline [0]_{13\times2} & [0]_{13\times2} & C_{\text{INVc3}} \end{array}\right]_{6\times39} \tag{5.69}$$

$$A_{\text{INV}} = \left[\begin{array}{c|c|c} A_{\text{INV1}} + B_{1\omega\text{com}}C_{\text{INV}\omega1} & [0]_{13\times13} & [0]_{13\times13} \\ \hline X_{m_p} & A_{\text{INV2}} + B_{2\omega\text{com}}C_{\text{INV}\omega2} & [0]_{13\times13} \\ \hline X_{m_p} & [0]_{13\times13} & A_{\text{INV}k} + B_{k\omega\text{com}}C_{\text{INV}\omega k} \end{array}\right]_{39\times39}. \tag{5.70}$$

5.5.6 Line and Load Models

This subsection presents the generic state-space small-signal models of n lines and p loads of the study microgrid; both of which are modeled with lumped RL circuits, see Fig. 5.5. The generic small-signal state-space model of the lines of the microgrid (network) reads [10]

$$[\Delta\dot{i}_{\text{Line}DQ}] = A_{\text{NET}}[\Delta i_{\text{Line}DQ}] + B_{1\text{NET}}[\Delta v_{bDQ}] + B_{2\text{NET}}\Delta\omega_{com}, \tag{5.71}$$

where

$$A_{\text{NET}} = \text{diag}([A_{\text{NET1}}, A_{\text{NET1}}, \ldots, A_{\text{NET}n}])_{2n\times2n} \tag{5.72}$$

$$A_{\text{NET}i} = \begin{bmatrix} \frac{-R_{\text{LINE}i}}{L_{\text{LINE}i}} & \omega_0 \\ -\omega_0 & \frac{-R_{\text{LINE}i}}{L_{\text{LINE}i}} \end{bmatrix} \tag{5.73}$$

$$B_{1\text{NET}} = [B_{1\text{NET1}}\ B_{1\text{NET2}} \ldots B_{1\text{NET}n}]^T_{2n\times2m} \tag{5.74}$$

$$B_{1\text{NET}i} = \begin{bmatrix} \ldots & \frac{1}{L_{\text{LINE}i}} & 0 & \ldots & \frac{-1}{L_{\text{LINE}i}} & 0 & \ldots \\ \ldots & 0 & \frac{1}{L_{\text{LINE}i}} & \ldots & 0 & \frac{-1}{L_{\text{LINE}i}} & \ldots \end{bmatrix}_{2\times2m} \tag{5.75}$$

$$B_{2\text{NET}} = [B_{2\text{NET1}}\ B_{2\text{NET2}} \ldots B_{2\text{NET}n}]^T_{2n\times1} \tag{5.76}$$

$$B_{2\text{NET}i} = [I_{\text{Line}Qi}\ -I_{\text{Line}Di}]^T_{1\times2} \tag{5.77}$$

Applying these small-signal models to the two lines (line 1 and line 2) of the study microgrid system shown in Fig. 5.5 yields:

$$A_{\mathrm{NET}} = \begin{bmatrix} \begin{bmatrix} \frac{-R_{\mathrm{LINE1}}}{L_{\mathrm{LINE1}}} & \omega_0 \\ -\omega_0 & \frac{-R_{\mathrm{LINE1}}}{L_{\mathrm{LINE1}}} \end{bmatrix} & [0]_{2\times 2} \\ [0]_{2\times 2} & \begin{bmatrix} \frac{-R_{\mathrm{LINE2}}}{L_{\mathrm{LINE2}}} & \omega_0 \\ -\omega_0 & \frac{-R_{\mathrm{LINE2}}}{L_{\mathrm{LINE2}}} \end{bmatrix} \end{bmatrix}_{4\times 4} \tag{5.78}$$

$$B_{1\mathrm{NET}} = \begin{bmatrix} \frac{1}{L_{\mathrm{LINE1}}} & 0 & \frac{-1}{L_{\mathrm{LINE1}}} & 0 & 0 & 0 \\ 0 & \frac{1}{L_{\mathrm{LINE1}}} & 0 & \frac{-1}{L_{\mathrm{LINE1}}} & 0 & 0 \\ 0 & 0 & \frac{1}{L_{\mathrm{LINE2}}} & 0 & \frac{-1}{L_{\mathrm{LINE2}}} & 0 \\ 0 & 0 & 0 & \frac{1}{L_{\mathrm{LINE2}}} & 0 & \frac{-1}{L_{\mathrm{LINE2}}} \end{bmatrix}_{4\times 6} \tag{5.79}$$

$$B_{2\mathrm{NET}} = \begin{bmatrix} I_{\mathrm{LineQ1}} \\ -I_{\mathrm{LineD1}} \\ I_{\mathrm{LineQ2}} \\ -I_{\mathrm{LineD2}} \end{bmatrix}_{4\times 1}. \tag{5.80}$$

Similar to Equation 5.71, the generic small-signal state-space model of the loads is

$$[\Delta \dot{i}_{\mathrm{Load}DQ}] = A_{\mathrm{LOAD}}[\Delta i_{\mathrm{Load}DQ}] + B_{1\mathrm{LOAD}}[\Delta v_{bDQ}] + B_{2\mathrm{LOAD}}\Delta\omega_{com}, \tag{5.81}$$

where

$$A_{\mathrm{LOAD}} = \mathrm{diag}(\left[A_{\mathrm{LOAD1}}, A_{\mathrm{LOAD2}}, \ldots, A_{\mathrm{LOAD}p}\right])_{2p\times 2p} \tag{5.82}$$

$$A_{\mathrm{LOAD}i} = \begin{bmatrix} \frac{-R_{\mathrm{LOAD}i}}{L_{\mathrm{LOAD}i}} & \omega_0 \\ -\omega_0 & \frac{-R_{\mathrm{LOAD}i}}{L_{\mathrm{LOAD}i}} \end{bmatrix} \tag{5.83}$$

$$B_{1\mathrm{LOAD}} = \left[B_{1\mathrm{LOAD1}}\ B_{1\mathrm{LOAD2}} \ldots B_{1\mathrm{LOAD}p}\right]^T_{2p\times 2m} \tag{5.84}$$

$$B_{1\mathrm{LOAD}i} = \begin{bmatrix} \dots & \frac{1}{L_{\mathrm{LOAD}i}} & 0 & \dots \\ \dots & 0 & \frac{1}{L_{\mathrm{LOAD}i}} & \dots \end{bmatrix}_{2\times 2m} \tag{5.85}$$

$$B_{2\mathrm{LOAD}} = \begin{bmatrix} B_{2\mathrm{LOAD}1} & B_{2\mathrm{LOAD}2} & \dots & B_{2\mathrm{LOAD}p} \end{bmatrix}^T_{2p\times 1} \tag{5.86}$$

$$B_{2\mathrm{LOAD}i} = \begin{bmatrix} I_{\mathrm{Load}Qi} & -I_{\mathrm{Load}Di} \end{bmatrix}^T_{1\times 2}. \tag{5.87}$$

Applying these small-signal models to the two loads (load 1 and load 3) of study microgrid system shown in Fig. 5.5 yields:

$$A_{\mathrm{LOAD}} = \begin{bmatrix} \begin{bmatrix} \frac{-R_{\mathrm{LOAD}1}}{L_{\mathrm{LOAD}1}} & \omega_0 \\ -\omega_0 & \frac{-R_{\mathrm{LOAD}1}}{L_{\mathrm{LOAD}1}} \end{bmatrix} & [\mathbf{0}]_{2\times 2} & [\mathbf{0}]_{2\times 2} \\ [\mathbf{0}]_{2\times 2} & [\mathbf{0}]_{2\times 2} & [\mathbf{0}]_{2\times 2} \\ [\mathbf{0}]_{2\times 2} & [\mathbf{0}]_{2\times 2} & \begin{bmatrix} \frac{-R_{\mathrm{LOAD}3}}{L_{\mathrm{LOAD}3}} & \omega_0 \\ -\omega_0 & \frac{-R_{\mathrm{LOAD}3}}{L_{\mathrm{LOAD}3}} \end{bmatrix} \end{bmatrix}_{6\times 6} \tag{5.88}$$

$$B_{1\mathrm{LOAD}} = \begin{bmatrix} \frac{1}{L_{\mathrm{LOAD}1}} & 0 & 0 & 0 & 0 & 0 \\ 0 & \frac{1}{L_{\mathrm{LOAD}1}} & 0 & 0 & 0 & 0 \\ 0 & 0 & 0 & 0 & 0 & 0 \\ 0 & 0 & 0 & 0 & 0 & 0 \\ 0 & 0 & 0 & 0 & \frac{1}{L_{\mathrm{LOAD}3}} & 0 \\ 0 & 0 & 0 & 0 & 0 & \frac{1}{L_{\mathrm{LOAD}3}} \end{bmatrix}_{6\times 6} \tag{5.89}$$

$$B_{2\mathrm{LOAD}} = \begin{bmatrix} I_{\mathrm{LoadQ}1} \\ -I_{\mathrm{LoadD}1} \\ 0 \\ 0 \\ I_{\mathrm{LoadQ}3} \\ -I_{\mathrm{LoadD}3} \end{bmatrix}_{6\times 1}. \tag{5.90}$$

5.5.7 Complete Microgrid Model

The small-signal model of the node voltages in the microgrid can be written as [10]

$$[\Delta v_{bDQ}] = R_N(M_{\text{INV}}[\Delta i_{oDQ}] + M_{\text{LOAD}}[\Delta i_{\text{Load}DQ}] + M_{\text{NET}}[\Delta i_{\text{Line}DQ}]), \tag{5.91}$$

where $R_N = r_N \cdot [I]_{2m\times 2m}$, the mapping matrix $M_{\text{INV}} = [I]_{2m\times 2s}$ which maps the inverter connection points onto the network nodes. $[I]$ is the identity matrix and r_N is a large virtual resistor ($r_N = 1000\ \Omega$) introduced that all voltages in the system are well defined. $M_{\text{LOAD}2m\times 2p}$ maps load connection points onto the network nodes with -1, and $M_{\text{NET}2m\times 2n}$ maps the connecting lines onto the network nodes with ± 1, whether the current enters or exits the node.

Applying these small-signal models to the study microgrid system in Fig. 5.5 results in:

$$R_N = \begin{bmatrix} r_N & 0 & 0 & 0 & 0 & 0 \\ 0 & r_N & 0 & 0 & 0 & 0 \\ 0 & 0 & r_N & 0 & 0 & 0 \\ 0 & 0 & 0 & r_N & 0 & 0 \\ 0 & 0 & 0 & 0 & r_N & 0 \\ 0 & 0 & 0 & 0 & 0 & r_N \end{bmatrix}_{6\times 6} \tag{5.92}$$

$$M_{INV} = \begin{bmatrix} 1 & 0 & 0 & 0 & 0 & 0 \\ 0 & 1 & 0 & 0 & 0 & 0 \\ 0 & 0 & 1 & 0 & 0 & 0 \\ 0 & 0 & 0 & 1 & 0 & 0 \\ 0 & 0 & 0 & 0 & 1 & 0 \\ 0 & 0 & 0 & 0 & 0 & 1 \end{bmatrix}_{6\times 6} \tag{5.93}$$

$$M_{LOAD} = \begin{bmatrix} -1 & 0 & 0 & 0 & 0 & 0 \\ 0 & -1 & 0 & 0 & 0 & 0 \\ 0 & 0 & 0 & 0 & 0 & 0 \\ 0 & 0 & 0 & 0 & 0 & 0 \\ 0 & 0 & 0 & 0 & -1 & 0 \\ 0 & 0 & 0 & 0 & 0 & -1 \end{bmatrix}_{6\times 6} \tag{5.94}$$

$$M_{NET} = \begin{bmatrix} -1 & 0 & 0 & 0 \\ 0 & -1 & 0 & 0 \\ 1 & 0 & -1 & 0 \\ 0 & 1 & 0 & -1 \\ 0 & 0 & 1 & 0 \\ 0 & 0 & 0 & 1 \end{bmatrix}_{6\times 6}. \tag{5.95}$$

5.5.8 System Matrix

Finally, in this subsection, the previously derived small-signal state-space submodels that make up the microgrid (inverters, filters, lines, and loads) are combined to form the system matrix A_{MG}.

$$\begin{bmatrix} \Delta\dot{x}_{\mathrm{INV}} \\ \Delta\dot{i}_{\mathrm{Line}DQ} \\ \Delta\dot{i}_{\mathrm{Load}DQ} \end{bmatrix} = A_{\mathrm{MG}} \begin{bmatrix} \Delta x_{\mathrm{INV}} \\ \Delta i_{\mathrm{Line}DQ} \\ \Delta i_{\mathrm{Load}DQ} \end{bmatrix} \tag{5.96}$$

$$A_{\mathrm{MG}} = \left[\begin{array}{c|c|c} A_{\mathrm{INV}} + B_{\mathrm{INV}} R_N M_{\mathrm{INV}} C_{\mathrm{INV}c} & B_{\mathrm{INV}} R_N M_{\mathrm{NET}} & B_{\mathrm{INV}} R_N M_{\mathrm{LOAD}} \\ \hline B_{1\mathrm{NET}} R_N M_{\mathrm{INV}} C_{\mathrm{INV}c} + B_{2\mathrm{NET}} C_{\mathrm{INV}\omega} & A_{\mathrm{NET}} + B_{1\mathrm{NET}} R_N M_{\mathrm{NET}} & B_{1\mathrm{NET}} R_N M_{\mathrm{LOAD}} \\ \hline B_{1\mathrm{LOAD}} R_N M_{\mathrm{INV}} C_{\mathrm{INV}c} + B_{2\mathrm{LOAD}} C_{\mathrm{INV}\omega} & B_{1\mathrm{LOAD}} R_N M_{\mathrm{NET}} & A_{\mathrm{LOAD}} + B_{1\mathrm{LOAD}} R_N M_{\mathrm{LOAD}} \end{array}\right]_{49\times 49} \tag{5.97}$$

This matrix is used for the eigenvalue and sensitivity analysis presented in Section 5.6, where the eigenvalue locations of the system are studied and their movement subsequent to system parameter changes is investigated.

5.6 Eigenvalue and Sensitivity Analysis of the Study Microgrid

In this section, the location and behavior of the eigenvalues of a study microgrid subsequent to changes in power controller parameters are investigated. Furthermore, the sensitivity of different modes to state variables is studied by calculating participation factors.

Fig. 5.5 shows the study microgrid; it operates in the islanded mode, supplies two loads, and includes three DG units connected by two lines.

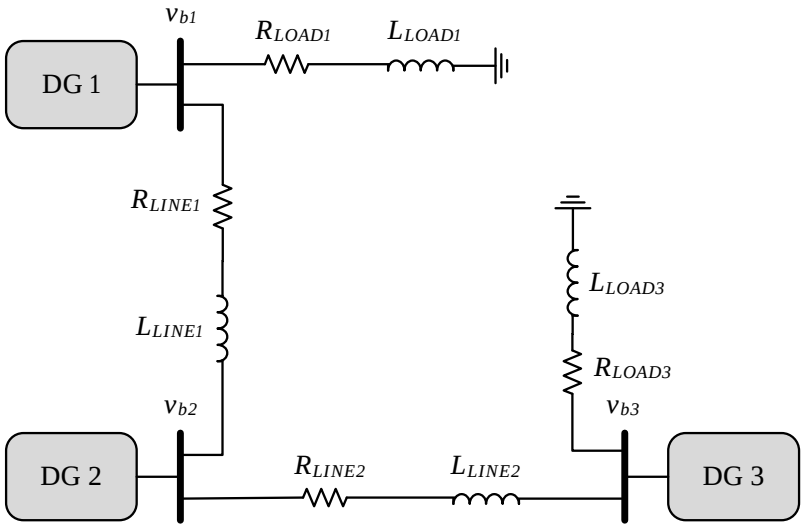

Figure 5.5: Study microgrid system.

Initial conditions, filter, line and controller parameters are selected to be the same as in [10] to facilitate the comparison. Table 5.1 shows the parameters of the study microgrid.

Table 5.1: Study System Parameters Part II

Parameter	Value	Parameter	Value	Parameter	Value
f	50 Hz	λ_c	10^{-5}	K'_{Iv}	78.5398
L_f	1.35 mH	λ_v	2×10^{-4}	R_{LOAD1}	25 Ω
R_f	0.1 Ω	T_c	2 ms	R_{LOAD3}	20 Ω
C_f	50 μF	K_{Pc}	135.625	R_{LINE1}	0.23 Ω
L_c	0.35 mH	K_{Ic}	9.1673×10^3	R_{LINE2}	0.35 Ω
R_c	0.03 Ω	K'_{Pc}	5.3014	L_{LOAD1}	10 nH
ω_c	31.41 rad/s	K'_{Ic}	4.2608×10^4	L_{LOAD3}	10 nH
m_p	9.4×10^{-5}	K_{Pv}	0.25	L_{LINE1}	318.31 μH
n_q	1.3×10^{-3}	K'_{Pv}	0.1571	L_{LINE2}	1.8 mH

5.6.1 Locus of Eigenvalues

The MATLAB function eig() is employed to calculate the eigenvalues of the system matrix A_{MG} and its corresponding right and left eigenvectors. Fig. 5.6 shows the locus of eigenvalues of the complete model of the study microgrid using both IMC and conventional PI-based controllers.

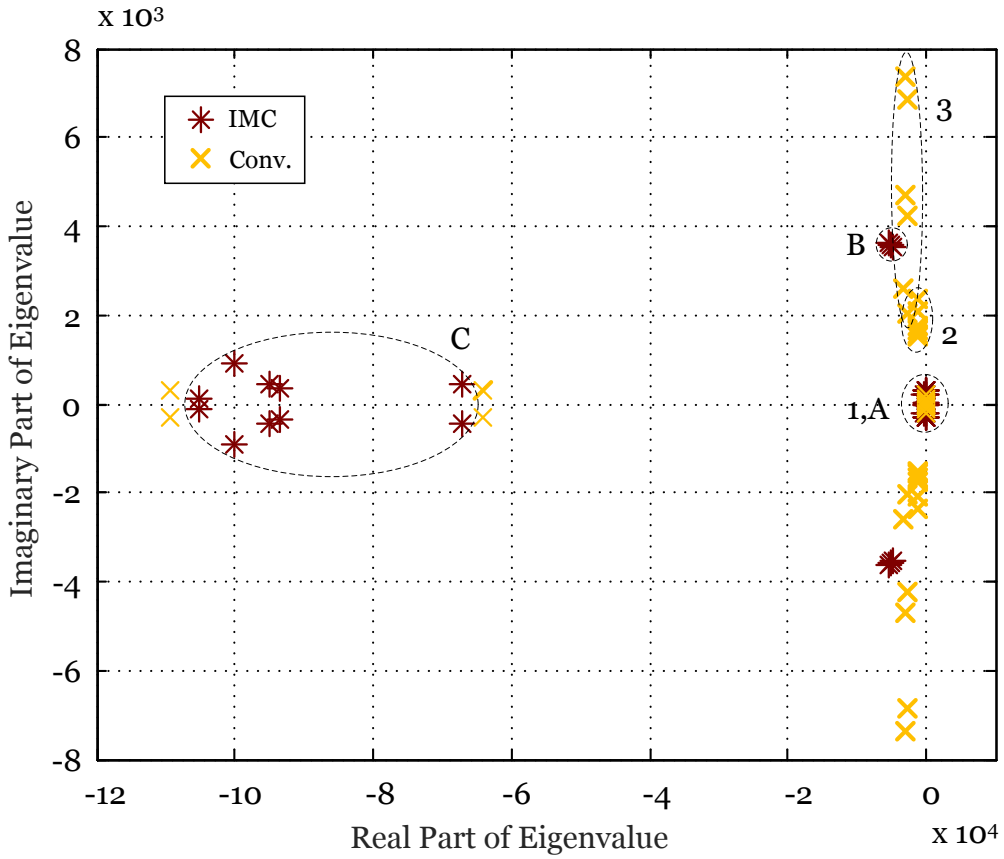

Figure 5.6: IMC vs. conventional method: Locus of eigenvalues of the study microgrid grouped into clusters (Fig. 5.7 shows a zoom of the clusters 1–3 and A–B for $-6000 \leq \mathrm{Re}\{\lambda\} \leq 1000$).

Fig. 5.7 shows a zoom of the clusters 1–3 and A–B for $-6000 \leq \mathrm{Re}\{\lambda\} \leq 1000$.

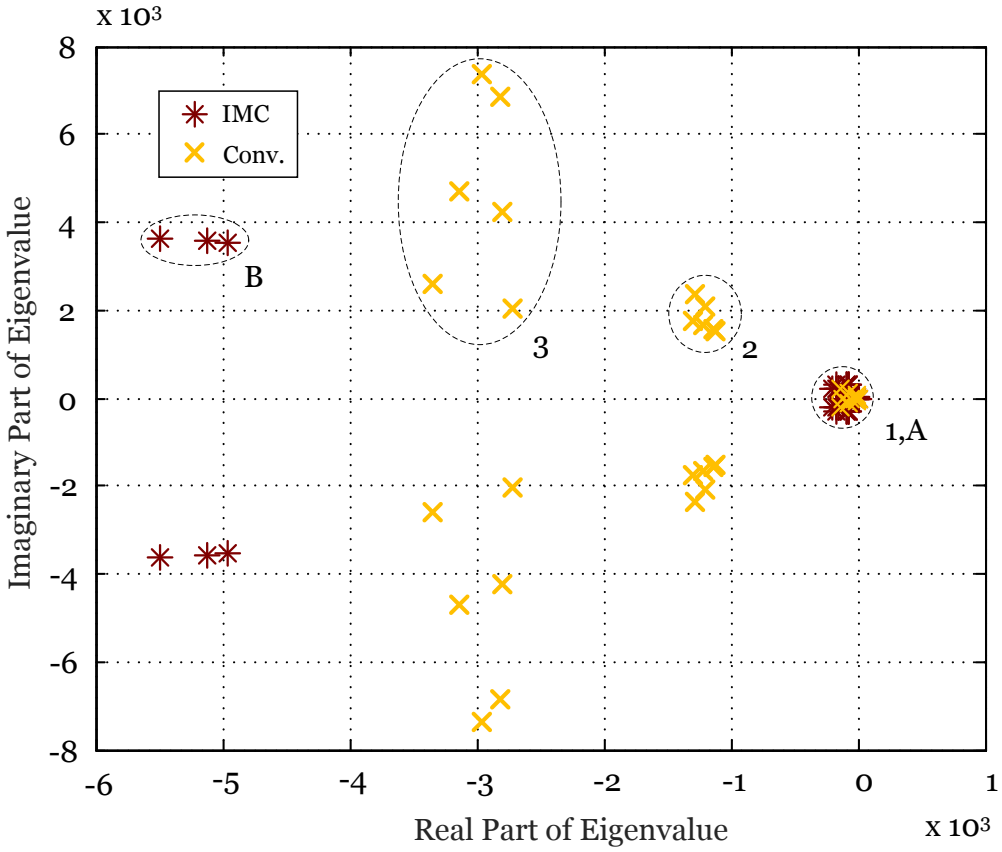

Figure 5.7: IMC vs. conventional method: Locus of eigenvalues of the study microgrid grouped into clusters (zoom of Fig. 5.6).

The complete system has eigenvalue clusters A, B, and C with IMC controllers, and eigenvalue clusters 1, 2, and 3 with PI controllers. Similar to the conventional PI-based approach, the IMC eigenvalues form a low-frequency cluster near the origin (cluster A in Figs. 5.6 and 5.7). However, it can be seen that the IMC clusters B and C have significantly improved damping ratios compared with clusters 2 and 3 of the conventional method. Cluster A, on the other hand, features more low-frequency eigenvalues than cluster 1 and is therefore studied in Subsections 5.6.2 and 5.6.3 in more detail (see Figs. 5.8 and 5.9).

The participation factor relating the kth state variable to the ith eigenvalue, in a system with a total of n eigenvalues, is defined as

$$p_{ki} = \frac{\lambda_i}{a_{kk}} = \frac{|v_{ki}||w_{ki}|}{\sum_{k=1}^{n} |v_{ki}||w_{ki}|}, \tag{5.98}$$

where λ_i is the ith eigenvalue, a_{kk} is a diagonal element of the system matrix, and w_{ki} and v_{ki} are the kth elements of the left and right eigenvectors associated with the ith eigenvalue [45]. The participation factors of the most critical modes λ_{1-2} and λ_{1-3}, where the subscripts indicate which inverters are affected the most, are listed in Table 5.2.

Table 5.2: Sensitivity of Critical IMC Low-Frequency Dominant Modes

Sensitivity of λ_{1-2}		Sensitivity of λ_{1-3}	
State	Participation	State	Participation
P_1	0.313	P_1	0.236
Q_1	0.109	Q_1	0.091
P_2	0.375	P_2	0.148
Q_2	0.106	P_3	0.384
P_3	0.066	Q_3	0.116

The participation factors show that, similar to the conventional approach studied in [10], low-frequency modes in cluster A are largely sensitive to the state variables of the power controller. Cluster B contains high-frequency modes sensitive to power controller state variables and output voltage Δv_{odq}, where the latter is a state variable of the filter and indirectly influences the state variables of the voltage controller, see Equations 5.3 and 5.4. High-frequency modes in cluster C are sensitive to state variables of the filter and indirectly affect the state variables of the current controller, see Equations 5.1 and 5.2.

5.6.2 Eigenvalue Sensitivity to Real Power Droop Gain

This subsection studies the sensitivity of the eigenvalues to the real power droop gain m_p to evaluate and compare the robustness and stability of both methods. For this purpose, the real power droop gain is varied between $1.57 \times 10^{-5} \leq m_p \leq 3.14 \times 10^{-4}$ and Fig. 5.8 shows the corresponding locus of low-frequency modes. The two critical eigenvalues of the sensitivity analysis listed in Table 5.2 are marked.

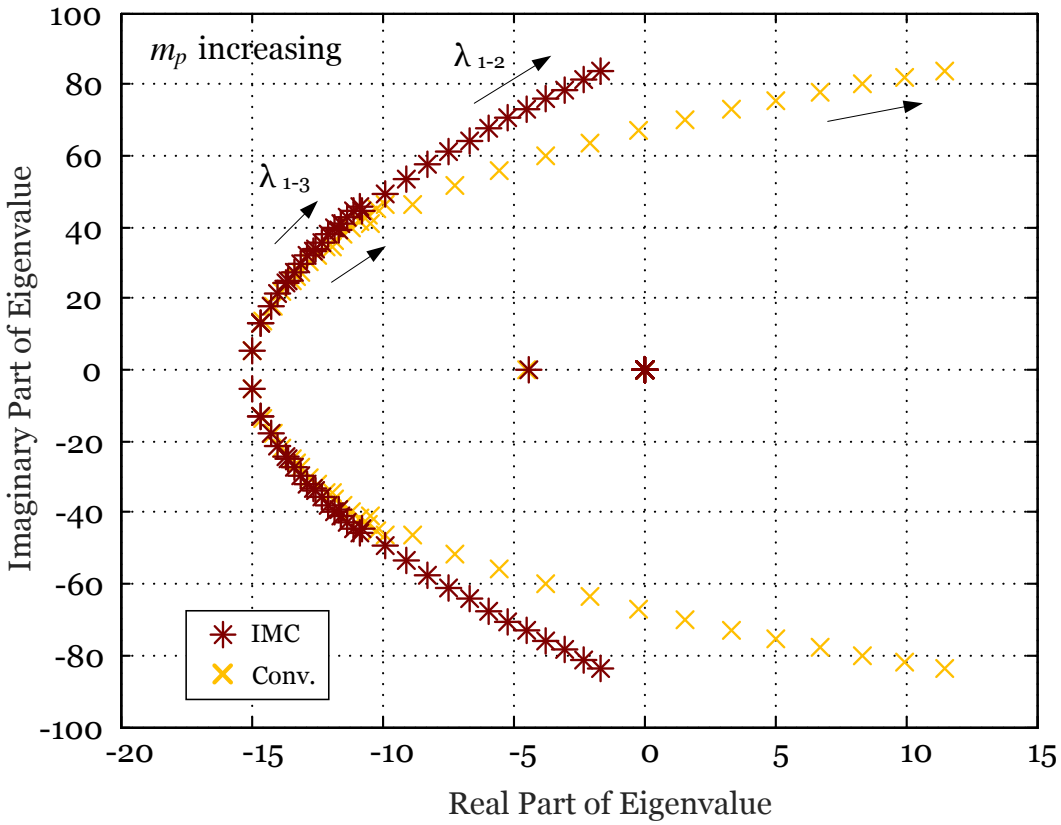

Figure 5.8: IMC vs. conventional method: Locus of low-frequency modes as a function of real power droop gain (for $1.57 \times 10^{-5} \leq m_p \leq 3.14 \times 10^{-4}$).

While the eigenvalues of the conventional control method deeply enter the right half plane and therefore become unstable, IMC eigenvalues remain in the left half plane and retain stability. Fig. 5.8 confirms that the IMC approach has superior stability performance compared with the conventional approach.

5.6.3 Eigenvalue Sensitivity to Reactive Power Droop Gain

In this subsection, the sensitivity of eigenvalues to the reactive power droop gain n_q is studied. Fig. 5.9 shows the locus of eigenvalues near the origin subsequent to a change in reactive power droop gain in the range of $3.17 \times 10^{-4} \leq n_q \leq 7 \times 10^{-3}$.

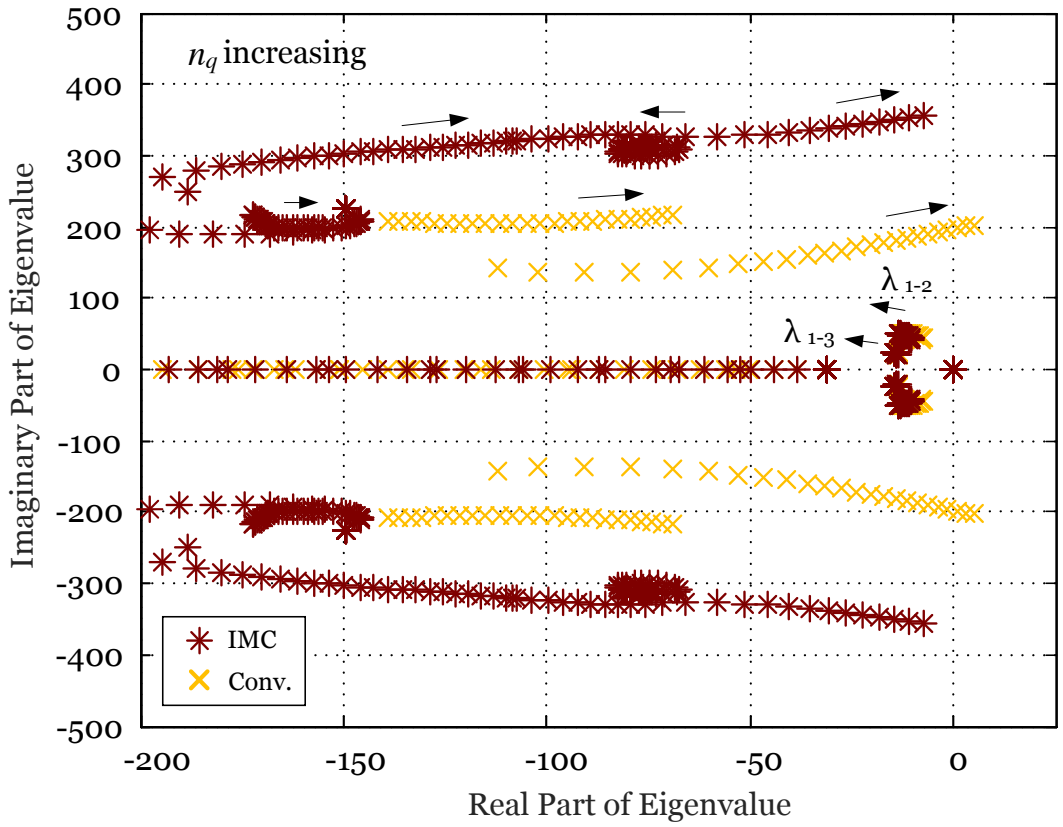

Figure 5.9: IMC vs. conventional method: Locus of low-frequency modes as a function of reactive power droop gain (for $3.17 \times 10^{-4} \leq n_q \leq 7 \times 10^{-3}$).

For IMC, eigenvalues located farther away from the real axis exhibit slightly larger imaginary parts compared with those of the conventional method. On the other hand, IMC eigenvalues located near the origin show slightly reduced real and imaginary parts with respect to magnitude as shown in Fig. 5.9. The eigenvalues of the conventional method become unstable by entering the right half plane while IMC eigenvalues remain in the left half plane and retain stability.

5.7 Simulation Results

This section discusses simulation case studies to evaluate the performance of the IMC-based control approach and the PI-based approach. The study microgrid shown in Figs. 5.1 and 5.5 is modeled in PSCAD/EMTDC environment. For the simulation case studies, the loads shown in Fig. 5.5 are excluded. Instead, for comparison with the results of [10], a large step change (from no load to 27 kW) is applied at bus 1 in order to pointedly capture the high-frequency modes which are dominated by the voltage and current controllers and not dominated by the power controller.

Figs. 5.10(a) and (b) show the real and reactive output power of the three DG units, respectively, caused by a 27 kW step change in load at bus 1, comparing IMC and the conventional method.

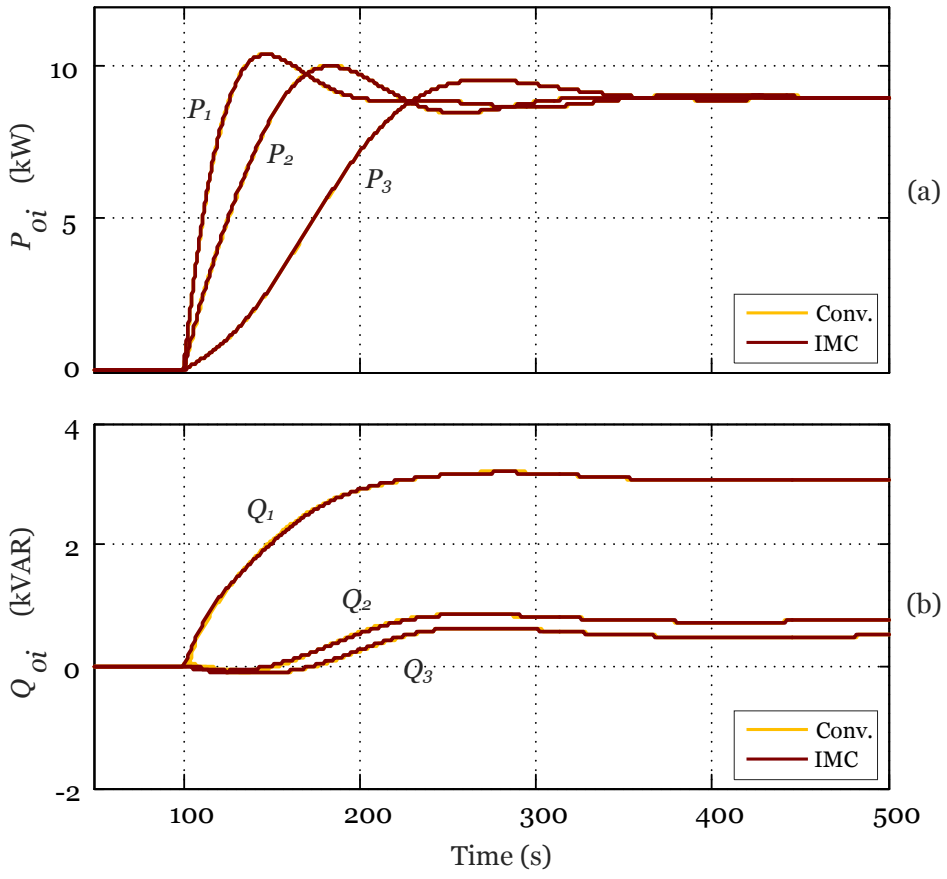

Figure 5.10: IMC vs. conventional method: Real and reactive output power responses of DG units ($i = 1, 2, 3$) subsequent to a 27 kW step change in load power at bus 1.

However, graphs of both methods overlap. As anticipated, both methods have similar results since they utilize the same power controller. It can be seen that low-frequency modes of around 7 Hz in cluster A dominate the transient response in real and reactive power, which agrees with results of [10]. Because no load is connected to the microgrid before $t = 0.1$ s, both the real output power and the reactive output power are zero. It can be seen that eventually the load of 27 kW is shared equally between the DG units. The DG unit with the shortest electrical distance from the load change responds the fastest but also shows the largest overshoot in its real power response. DG units inject reactive power according to the feeder impedance.

Figs. 5.11(a) and (b) illustrate the d- and q-components of the filter current i_l responses of the three DG units, respectively, comparing IMC and conventional methods.

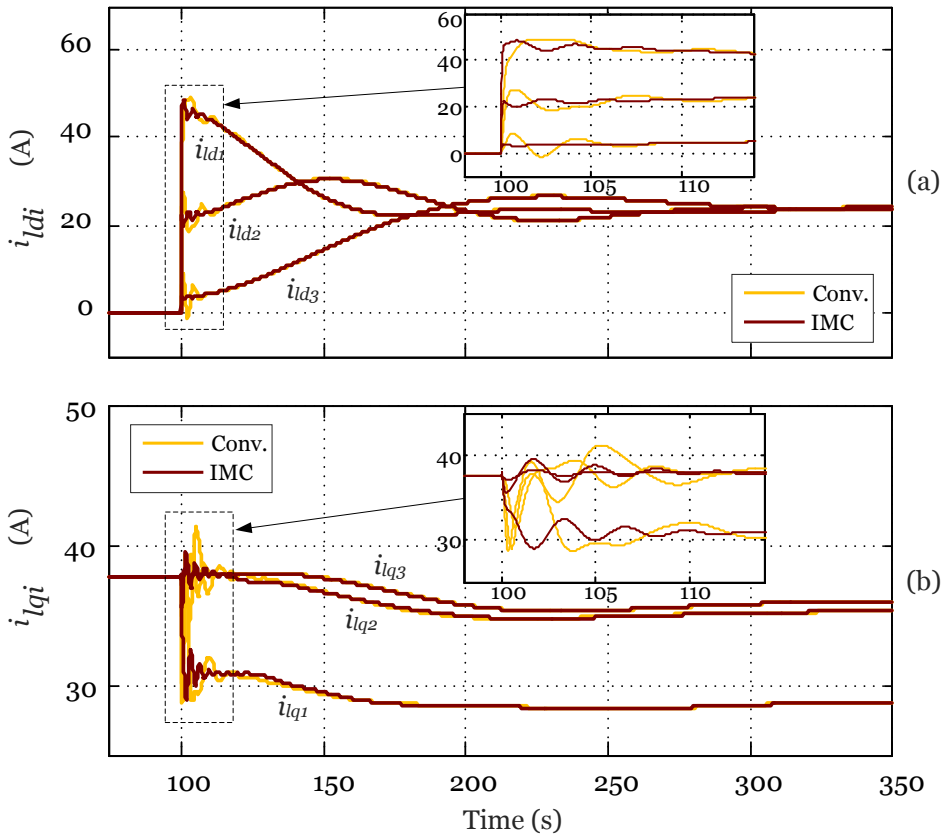

Figure 5.11: IMC vs. conventional method: Filter current (d- and q-axis) responses of DG units ($i = 1, 2, 3$) subsequent to a 27 kW step change in load power at bus 1.

Again, real power is shared equally since the d-components of the currents adjust to the same steady state value while q-components are according to reactive power sharing. Figs. 5.11(a) and (b) show that IMC has less overshoot and faster response than the conventional method, which agrees with [1,2].

Fig. 5.12 shows transient responses of DG unit output voltages v_{odi} ($i = 1,2,3$) induced by the applied load step change. It can be seen that IMC significantly reduces the transient voltage undershoot. The conventional method causes voltage undershoots up to 20%. However, the IMC-based method has a maximum voltage undershoot of only about 1.7%. This behavior agrees with the results of the single DG unit case presented in [1,2]. Reference [10] shows that the cluster 2 eigenvalues are responsible for the output voltage transients with frequencies around 350 Hz. IMC transients in the voltage show frequencies of around 1000 Hz and correspond to high-frequency modes in cluster B. Cluster B eigenvalues exhibit higher frequencies but have significantly improved damping ratios compared with cluster 2 eigenvalues. This explains the drastic reduction of voltage undershoot with IMC.

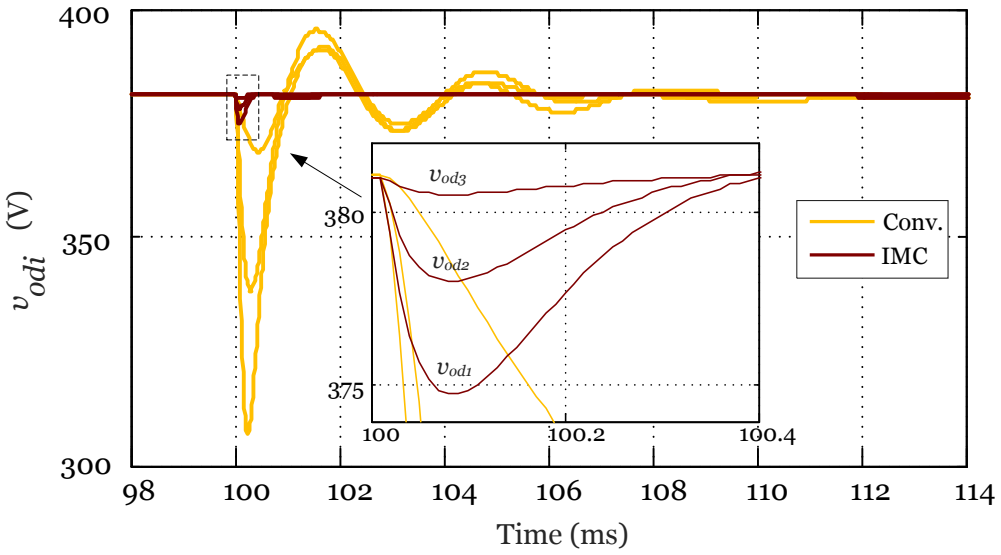

Figure 5.12: IMC vs. conventional method: Output voltage (d-axis) responses of DG units ($i = 1,2,3$) subsequent to a 27 kW step change in load power at bus 1.

It is important to point out that the waveforms of the PI-based approach start oscillating earlier than those of IMC as the real and reactive power droop gain coefficients m_p and n_q are increased (not displayed). This agrees with the results

of the small-signal analysis in Subsections 5.6.2 and 5.6.3, which predict that the conventional method becomes unstable earlier than the IMC method as m_p and n_q are increased (Figs. 5.8 and 5.9).

Chapter 6

Conclusion Part II

In this part of the thesis, a small-signal model of an inverter-based microgrid utilizing IMC-based controllers is derived. The model is used to perform eigenvalue and sensitivity analysis. Simulation case studies verify the results of this small-signal analysis. The results are compared with those of the same study microgrid utilizing conventional PI-based controllers.

Sensitivity analysis, employing the calculation of participation factors, shows that low-frequency modes are highly sensitive to the parameters of the power sharing controller of the DG units for both methods. Yet, the small-signal analysis finds the following:

- The roots for the drastically reduced voltage undershoot lie in the increased frequencies and damping ratios of sensitive eigenvalues; and
- By varying the droop coefficients m_p and n_q, compared with the PI-based approach, the study microgrid with IMC controllers exhibits superior stability performance.

Part III

Internal Model–Based Active Damping Current Control for a Grid-Connected Voltage Source Converter with an LCL Filter

The findings of Part III of this thesis have been submitted to *IEEE Transactions on Power Delivery* as Leitner *et al.* [5].

Chapter 7

Introduction Part III

Distributed generation (DG) units are usually interfaced to the grid via pulse-width modulated voltage-sourced converters (VSC) [31–33, 46]. Owing to the switches, VSCs produce sinusoidal waveforms that have harmonic components. Low-power applications with high switching frequencies can utilize simple L filters to reduce these switching harmonics. However, for high-power applications with low switching frequencies, L filters are costly and bulky [47–50] and LCL filters are utilized instead. The low-frequency behavior of an LCL filter is similar to that of an L filter but the LCL filter has improved damping performance at high frequencies. The downside of an LCL filter is the large peak at the resonance frequency in its frequency response. This resonance complicates the current control design to preserve the system stability [47, 50, 51]. Consequently, appropriate resonance damping methods should be employed for VSCs with LCL filters.

Significant research effort has been put into developing damping strategies to effectively deal with this resonance problem. Passive damping strategies, using physical resistors to pointedly dissipate power [48], are an effective means for low-cost low-power applications. However, medium- and high-power applications call for sophisticated active damping control strategies to improve efficiency, where the word active signifies that the VSC injects currents such that the resonance is not excited. Active damping strategies can be divided into two main categories [50]:

1. Additional feedback methods; and

2. High-order controllers (filters).

Category 1 control strategies usually require additional sensors, feeding back either the capacitor current or voltage to stabilize the system [47, 52–55]. As they

require additional measurements, both the cost and complexity of the system increase. While estimation-based sensorless active damping methods exist [51, 56], their performance is still not satisfactory. Category 2 control strategies usually use notch or biquad filters in series with the current controller to compensate for the resonance peak of the LCL filter [57–60]. These methods do not require additional measurements but often lack in robustness or bandwidth. Filter-based damping methods are especially desired when measurements of additional filter states are not possible (e.g., for cable-connected DG units). References [57, 59, 60] use proportional-resonance (PR) current controllers in series with high-order filters to regulate single-phase systems but [57] also uses PR controllers in a stationary reference frame for three-phase systems. Reference [58] utilizes proportional-integral (PI) current controllers plus a high-order filter (low-pass, lead, notch, or biquad) in each axis of a rotating reference frame.

Part III of this thesis proposes a high-order filter active damping current controller based on internal model control (IMC) for a grid-connected VSC with an LCL filter. The proposed controller is implemented in the rotating dq reference frame to allow independent control of injected three-phase real and reactive power. As opposed to the existing Category 2 methods, the IMC active damping controller 1) takes the decoupling terms for d and q axes into account to achieve better transient behavior, 2) is simultaneously both the controller and the filter due to the internal model principle, and 3) has a very simple design procedure with only one tuning parameter.

As its name implies, the IMC controller includes a model of the controlled plant and has the following characteristics:

- Increased robustness against system parameter changes;
- Improved transient behavior;
- Easy tuning with only one tuning parameter; and
- No need for additional sensors;

which significantly increase the system stability, facilitate the active damping of the LCL filters of a VSC, and keep the system cost low. Simulation case studies confirm these superior characteristics of the proposed IMC-based active damping current controller.

The rest of Part III of this thesis is organized as follows. In Chapter 8, the proposed IMC-based AD current controller is derived. A frequency response analysis of the

controller is presented in Chapter 9. Chapter 10 gives a short introduction to two existing active damping methods. In Chapter 11, the results of the time domain simulation case studies are discussed. Finally, Chapter 12 recapitulates Part III and draws conclusions.

Chapter 8

IMC-Based Active Damping Current Controller

This chapter shows the design procedure of the IMC-based active damping current controller shown in Fig. 8.1, given the plant model (LCL filter) and the IMC procedure presented in Section 3.2. As shown in Fig. 8.1, the controller inputs are the filter output voltage v_o and current i_2. The complex transfer functions in this chapter represent the rotating dq reference frame (RRF) and are marked with superscript dq. The acronym ESR stands for the equivalent series resistance of a inductance.

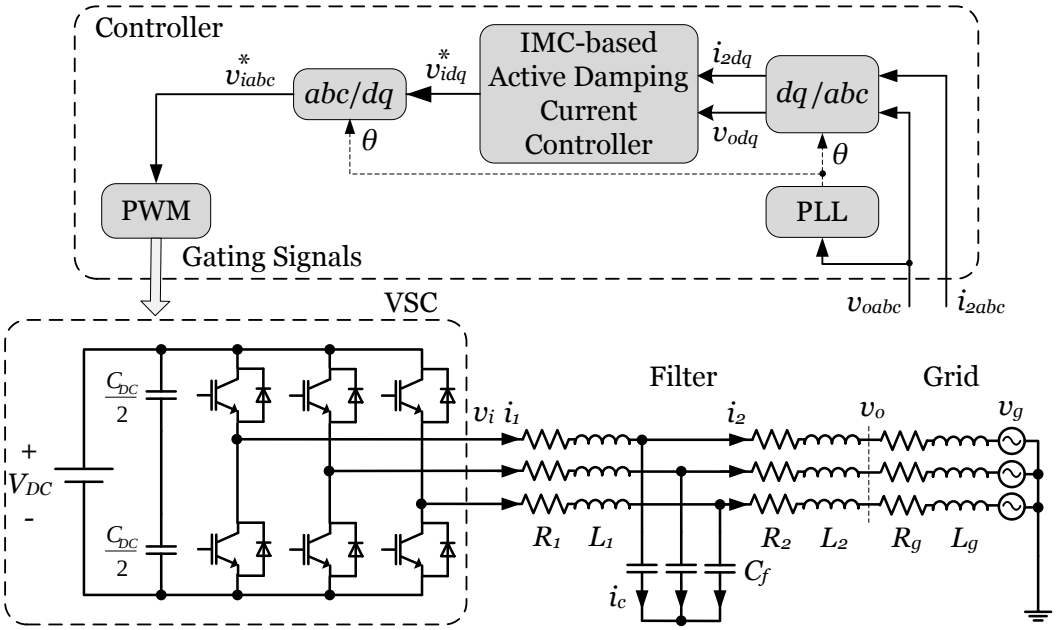

Figure 8.1: Block diagram of the DG unit including controller, VSC, LCL filter, and grid connection.

8.1 Controller Development

The resonance frequency of the system shown in Fig. 8.1 can be calculated as follows [50]:

$$f_{\text{res}} = \frac{\omega_{res}}{2\pi} = \sqrt{\frac{1}{C_f}\left(\frac{1}{L_1} + \frac{1}{L_2 + L_g}\right)}. \tag{8.1}$$

Fig. 8.2 shows the simplified block diagram of the system in Fig. 8.1.

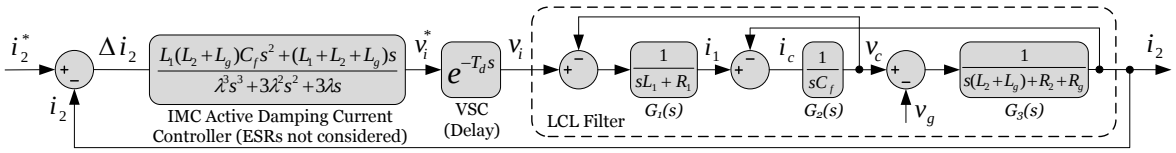

Figure 8.2: Simplified block diagram of the proposed IMC-based active damping current controller (ESRs are not considered), VSC, and LCL filter system.

8.1.1 Detailed Model

The current controller aims to control the DG unit output current i_2 by adjusting the inverter output voltage v_i. Applying basic block diagram reduction rules to the LCL filter transfer functions $G_1(s)$, $G_2(s)$, and $G_3(s)$ in Fig. 8.2 gives the LCL filter model (ESRs are considered):

$$\begin{aligned}\tilde{G}_P(s) = \frac{I_2(s)}{V_i(s)} &= \frac{G_1(s)G_2(s)G_3(s)}{1 + G_1(s)G_2(s) + G_2(s)G_3(s)} = \frac{\frac{1}{(sL_1+R_1)sC_f(s(L_2+L_g)+R_2+R_g)}}{1 + \frac{1}{(sL_1+R_1)sC_f} + \frac{1}{sC_f(s(L_2+L_g)+R_2+R_g)}} \\ &= \frac{1}{\alpha s^3 + \beta s^2 + \gamma s + \delta},\end{aligned} \tag{8.2}$$

where

$$\begin{cases} \alpha = L_1(L_2 + L_g)C_f \\ \beta = L_1C_f(R_2 + R_g) + R_1(L_2 + L_g)C_f \\ \gamma = R_1(R_2 + R_g)C_f + L_1 + L_2 + L_g \\ \delta = R_1 + R_2 + R_g. \end{cases} \tag{8.3}$$

To improve the accuracy of the model, the on-resistance r_{on} of the VSC switches can be added R_1. For the representation in RRF, the frequency shift $s \rightarrow s + j\omega$ is applied to the plant model in Equation 8.2:

$$\tilde{G}_P^{dq}(s) = \frac{1}{\alpha(s+j\omega)^3 + \beta(s+j\omega)^2 + \gamma(s+j\omega) + \delta}, \tag{8.4}$$

where ω is the angular speed of the RRF. Inserting Equation 8.4 into Equation 3.3 and selecting $n = 3$ to make the controller proper yields:

$$K^{dq}(s) = \frac{\alpha s^3 + \beta s^2 + (\gamma - 3\omega^2\alpha)s + (\delta - \omega^2\beta)}{s^3\lambda^3 + s^2 3\lambda^2 + 3\lambda s} + j\frac{3\alpha\omega s^2 + 2\omega\beta s + (\omega\gamma - \omega^3\alpha)}{s^3\lambda^3 + s^2 3\lambda^2 + 3\lambda s}, \tag{8.5}$$

where λ is the tuning parameter.

Fig. 8.3 shows the structure of the IMC-based active damping controller along with the LCL filter in the dq reference frame.

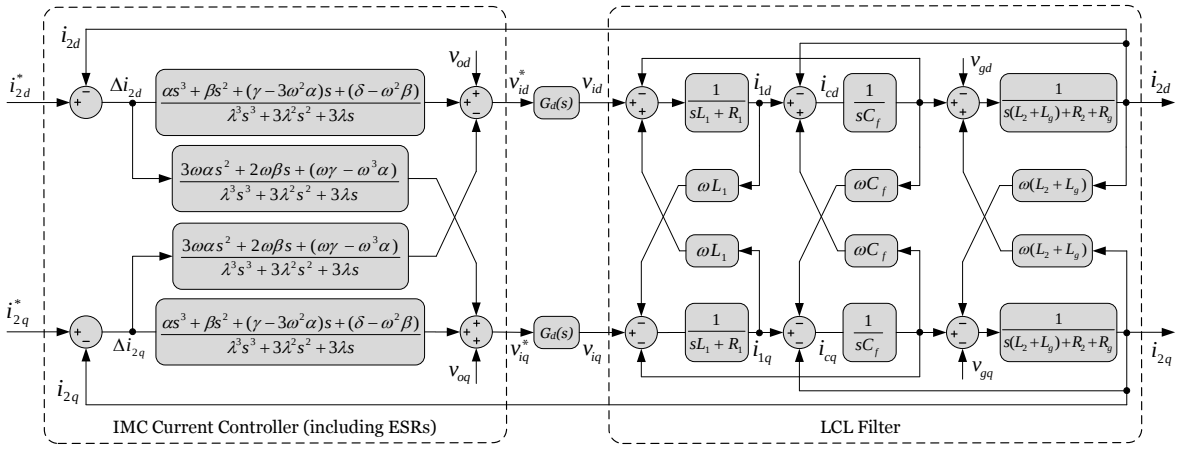

Figure 8.3: Block diagram of the IMC-based active damping current controller (ESRs are considered), VSC, and LCL filter model in the dq reference frame.

$G_d(s) = e^{-1.5s/f_{sw}}$ models the time delay of the VSC [55]. The IMC-based controller $K^{dq}(s)$ in Equation 8.5 represents a high-order multi-input multi-output (MIMO) controller and can be classified as a Category 2 control approach. However, compared to other Category 2 methods [57–60], $K^{dq}(s)$ is both the controller and the filter, with only one tuning parameter λ for both of them. The inner controller $G_C(s)$ is the inverse of the LCL filter model. Moreover, decoupling between d and q axes is taken into account. These characteristics make the performance of the proposed IMC-based active damping approach superior to existing methods.

8.1.2 Simplified Model

If the $\frac{R}{\omega L}$ ratio of the LCL filter is small, the control structure can be simplified. Setting the resistances R_1, R_2, and R_g in Equation 8.2 to zero yields the following transfer function for the LCL filter without ESRs [58, 61]:

$$G'_p(s) = \frac{1}{sL_1(L_2+L_g)C_f}\frac{1}{s^2+\omega_{res}^2} = \frac{1}{s(\alpha' s^2+\beta')}, \tag{8.6}$$

where considering (8.1) results in

$$\begin{cases} \alpha' = L_1(L_2+L_g)C_f \\ \beta' = L_1+L_2+L_g. \end{cases} \tag{8.7}$$

Applying the frequency shift $s \rightarrow s+j\omega$ to Equation 8.6 and substituting Equation 8.6 into Equation 3.3, results in the simplified MIMO control transfer function ($n = 3$):

$$K'^{dq}(s) = \underbrace{\left(\frac{s+j\omega}{s}\right)}_{\text{MIMO Controller}} \underbrace{\left(\frac{(\alpha' s^2+\beta'-\alpha'\omega^2)+j(2\alpha'\omega s)}{s^2\lambda^3+s3\lambda^2+3\lambda}\right)}_{\text{MIMO Filter}}. \tag{8.8}$$

Fig. 8.4 shows the block diagram of this simplified controller which will be used for frequency-domain analysis in Chapter 9.

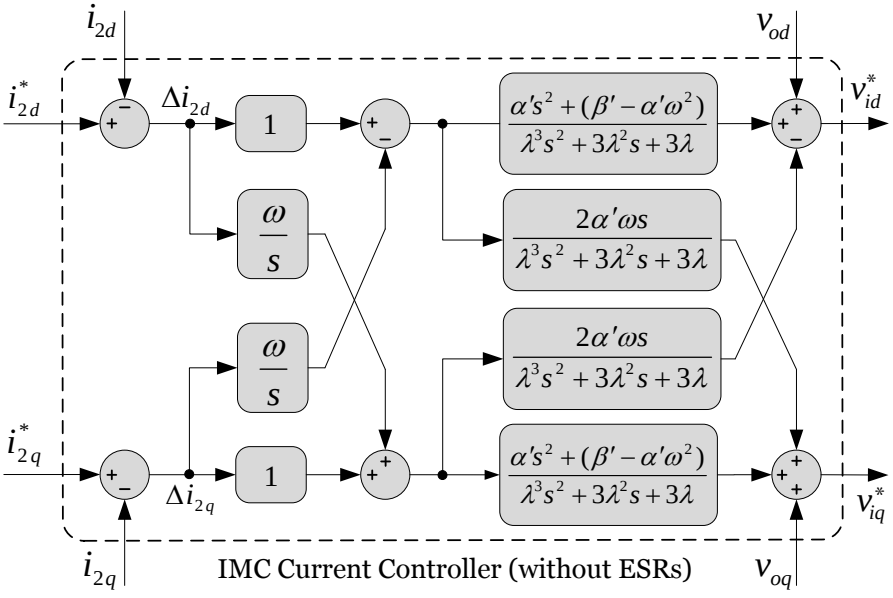

Figure 8.4: Block diagram of the IMC-based active damping current controller in the dq reference frame (ESRs are not considered).

Chapter 9

Frequency Domain Analysis

This chapter studies the frequency responses of the LCL filter, the proposed IMC-based active damping current controller, and their combination. The parameters of the LCL filter are listed in Table 9.1 and taken from [50] which provides typical filter values for medium-power applications.

Table 9.1: Study System Parameters Part III

Parameter	Value	Parameter	Value	Parameter	Value
f	60 Hz	f_{sw}	3780Hz	λ	0.0006
L_1, L_2	1.8 mH	R_1, R_2	0.1Ω	K_{rc}	15
L_g	2.5 mH	R_g	0.4Ω	ω_{rc}	$0.2\omega_{sw}$
C_f	27 μF	V_g	480 V	D_z	12.6381
C_{DC}	19280 μF	V_{DC}	1200 V	D_p	10039

The bode plots are drawn based on the simplified control loop for the DG unit output current i_2 in Fig. 8.2, which does not take the dq coupling terms in Equation 8.8 into account. The VSC is modeled with a time delay $T_d = 1.5/f_{sw}$ [55]. For demonstration purposes, the ESRs of the LCL filter are neglected.

9.1 Bode Plots

In the following, the frequency response of the IMC-based controller $K(s)$ subsequent to a change in the order of its low-pass filter $G_{\text{LPF}}(s)$ ($n = 3, 4, 5$) is investigated. Furthermore, the effect of the tuning parameter λ on the open-loop transfer function of Fig. 8.2 is studied.

Fig. 9.1 shows the bode plots of the LCL filter and IMC-based active damping controller for different orders of n and $\lambda = 0.0007$.

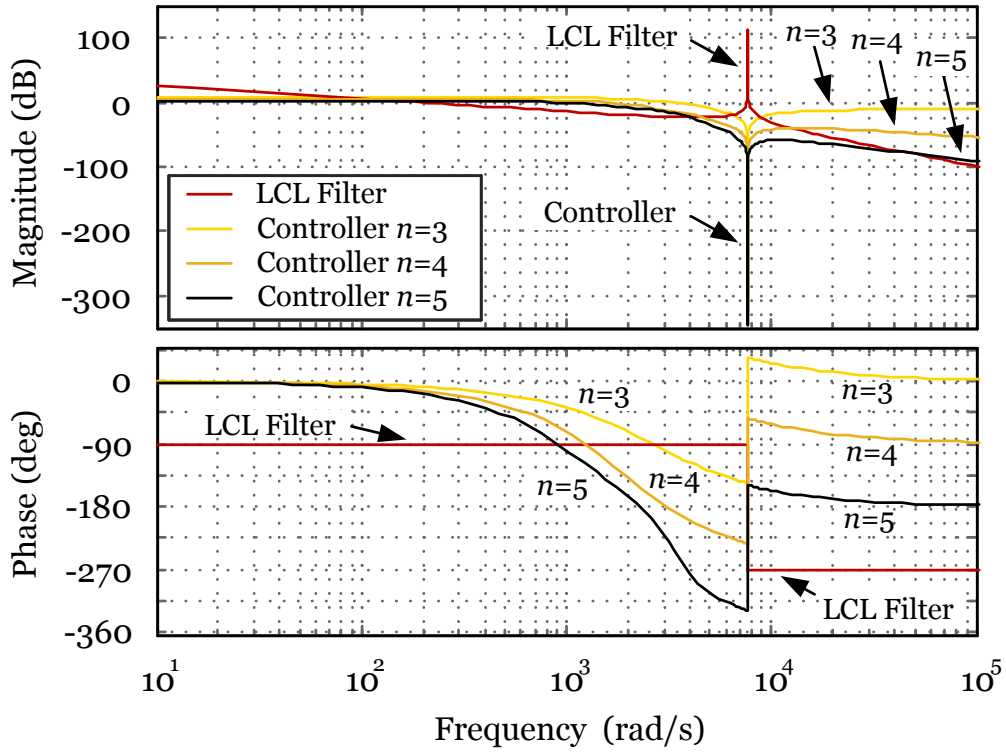

Figure 9.1: Frequency responses of the LCL filter and different orders of the IMC controller ($n = 3, 4, 5$) when ESRs are neglected and $\lambda = 0.0007$.

As expected, the LCL filter shows a high magnitude peak and a sharp phase drop from $-90°$ to $-270°$ at the resonance frequency (in case ESRs are considered, the resonance peak is smaller and the phase drops more smoothly). Fig. 9.1 shows that the proposed controller, which is according to the internal model principle designed to be the inverse of the plant, produces an anti-resonance (sharp amplitude dip) at the resonance frequency for all orders of $G_{\mathrm{LPF}}(s)$. As the order of $G_{\mathrm{LPF}}(s)$ increases, the bandwidth slightly decreases and the attenuation of high frequencies increases (both high bandwidth and high attenuation of the switching frequency are desirable). There is a tradeoff between the speed of the system and its harmonic rejection capability. As expected, increasing the order of $G_{\mathrm{LPF}}(s)$ also adds an additional $-90°$ per increased order to the phase.

Fig. 9.2 shows the bode plots of the open-loop transfer function of the circuit in Fig. 8.2 when ESRs are neglected.

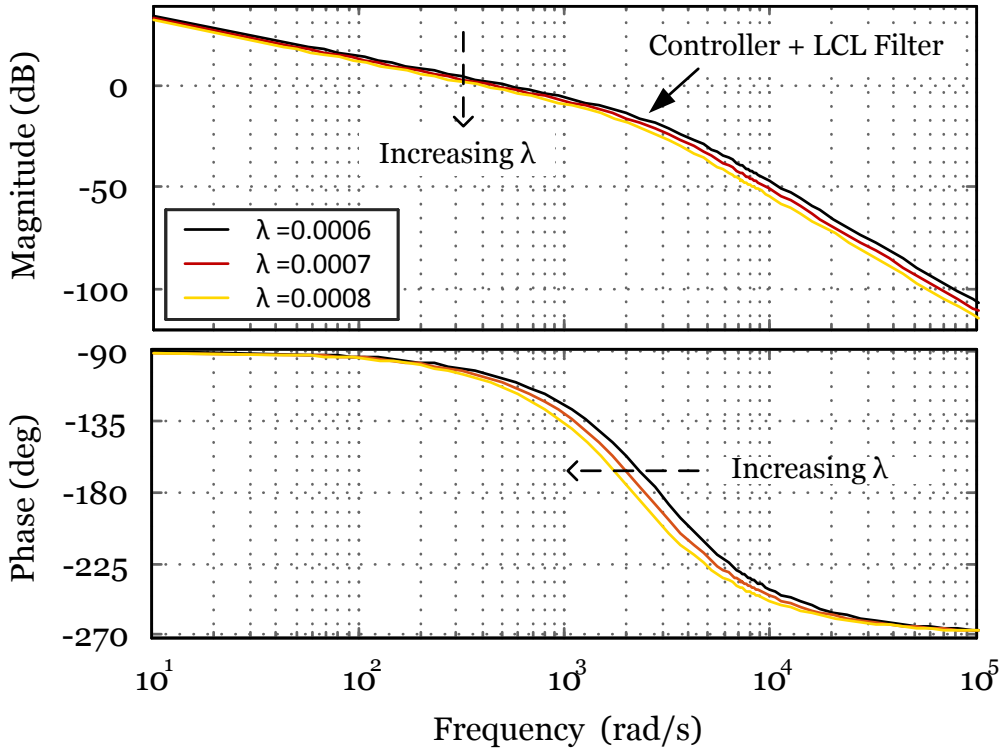

Figure 9.2: Frequency response of the open-loop transfer function of the simplified block diagram shown in Fig. 8.2 when ESRs are neglected ($n = 3$).

The change in frequency response is shown for $0.0006 \leq \lambda \leq 0.0008$ ($G_{\text{LPF}}(s)$ with $n = 3$). It is evident that the controller successfully compensates for the resonance peak of the LCL filter. As λ increases, the bandwidth decreases and the controller becomes slower. On the other hand, the attenuation of higher frequencies increases, which improves damping of switching harmonics. Similar to the choice of n in Fig. 9.1, the choice of λ is a tradeoff between the speed of the system and its harmonic rejection capability.

Chapter 10

Other Active Damping Methods

This chapter provides an overview of two selected active damping methods to compare with the proposed IMC-based active damping current controller. From Category 1 (additional feedback) methods, the virtual RC damping method [55] is chosen which measures and feeds back the capacitor current. From Category 2 (high-order filter) methods, the notch filter–based approach with a PI controller [58] is used.

Both methods are implemented with conventional PI controllers in the dq reference frame. To achieve the best transient behavior, decoupling and voltage feedforward terms are included. For low-frequency dynamics, the LCL filter can be approximated with a simple L filter [48]. Taking ESRs into account, the best results are obtained when controllers are tuned to attain zero-pole cancellation [1,62] with $R = R_1+R_2+R_g$, $L = L_1 + L_2 + L_g$, and $\tau = L/R$ (also considered was the symmetrical optimum tuning method for PI controllers [49, 63]).

10.1 Virtual RC Damping

Split capacitor damping is an established passive damping method in which the filter capacitor is paralleled with a series RC network to increase damping while keeping the power dissipation relatively low. As a further development of the virtual R damping method in [52], reference [55] proposed a virtual RC active damping strategy. This method measures the capacitor current and feeds it back through a high-pass filter to add damping. The high-pass filter acts like a virtual RC network in parallel to the filter capacitor.

Fig. 10.1 shows the block diagram of the implementation of the virtual *RC* damping method.

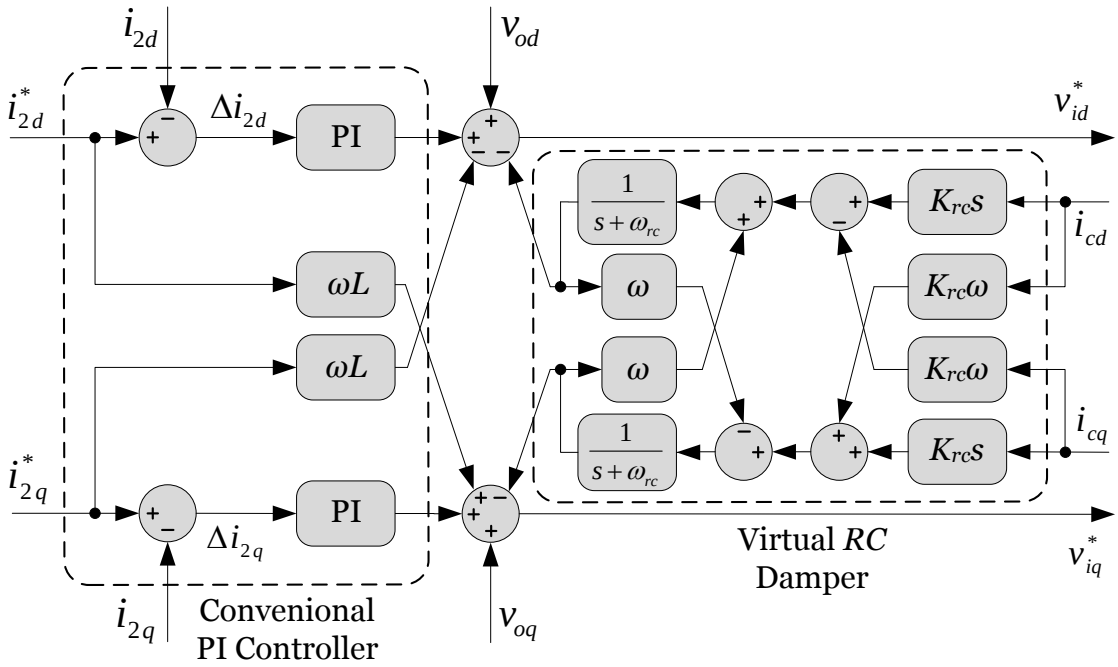

Figure 10.1: Block diagram of the virtual *RC* damping method combined with conventional PI current controllers in the *dq* reference frame, including cross-coupling and voltage feedforward terms.

The best results are obtained when the high-pass filter of the virtual *RC* method $\frac{sK_{rc}}{s+\omega_{rc}}$ is implemented with $K_{rc} = 15$ and $\omega_{rc} = 0.2\omega_{sw}$.

10.2 Notch Filter Damping

The notch filter–based active damping approach [58] utilizes a notch filter cascaded with a conventional PI current controller. The notch filter compensates the resonance peak of the LCL filter with an anti-resonance at the same frequency. This method is in general very frequency selective; hence, it is necessary to adjust the depth and width of the notch filter to increase robustness. However, a broader filter characteristic reduces the bandwidth of the controller.

Fig. 10.2 shows the block diagram of the implementation of the notch filter damping method.

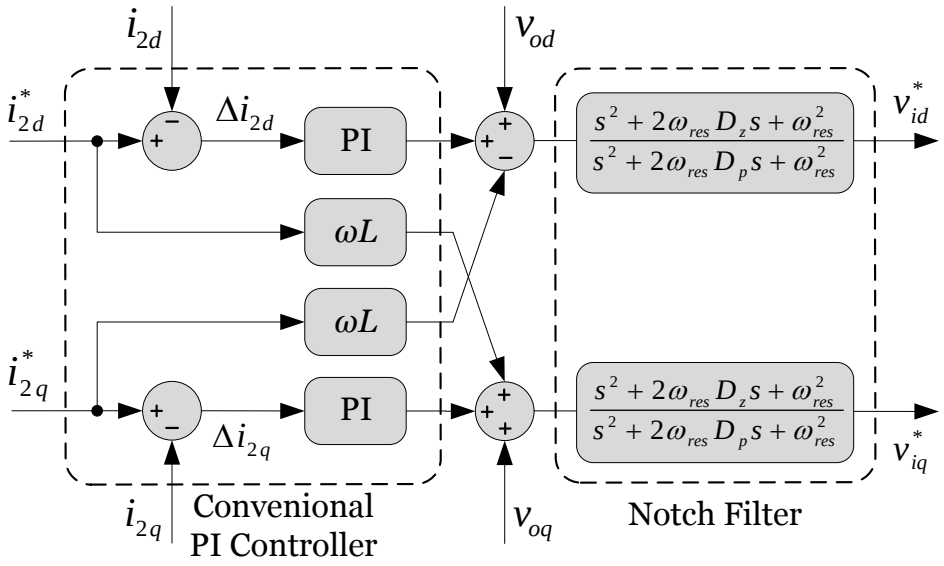

Figure 10.2: Block diagram of the notch filters combined with conventional PI current controllers in the dq reference frame, including cross-coupling and voltage feedforward terms.

The notch filter coefficients D_z and D_p are listed in Table 9.1 and tuned based on the resonance peak magnitude a_{peak} of the LCL filter including ESRs (see Figs. 8.1 and 8.2), with recommended 10% robustness [58]. Hence, filter parameter changes resulting in resonance frequency shifts of ±10% ($\Delta\omega = 0.1\omega_{res}$) are covered, while acceptable dynamic behavior is retained.

Chapter 11

Time Domain Simulations

This chapter discusses simulation case studies to evaluate the transient performance and robustness of the proposed IMC-based active damping current controller. The study system shown in Fig. 8.1 is modeled in PSCAD/EMTDC environment with the system parameters in Table 9.1. The results are compared with the two methods discussed in Chapter 10: virtual RC damping method (see Fig. 10.1) and the notch filter–based damping approach (see Fig. 10.2). The three studied methods are tuned to have similar rise times, settling times, and d-component overshoots.

As waveforms exhibit distortion during the robustness tests, the total harmonic distortion (THD) of the injected current i_2 is defined as an indicator of power quality degradation:

$$\mathrm{THD}_{63} = \sqrt{\sum_{h=2}^{63} \left(\frac{I_h}{I}\right)^2}. \tag{11.1}$$

11.1 Transient Performance

This section studies the transient behavior of the injected currents of the virtual RC, the notch filter, and the proposed IMC-based active damping methods.

Fig. 11.1 shows the dq-components of the current i_2 of the three tested methods for a step change from 50 A to 100 A in the d-component at $t = 0.1$ s, while the q-component is kept at zero.

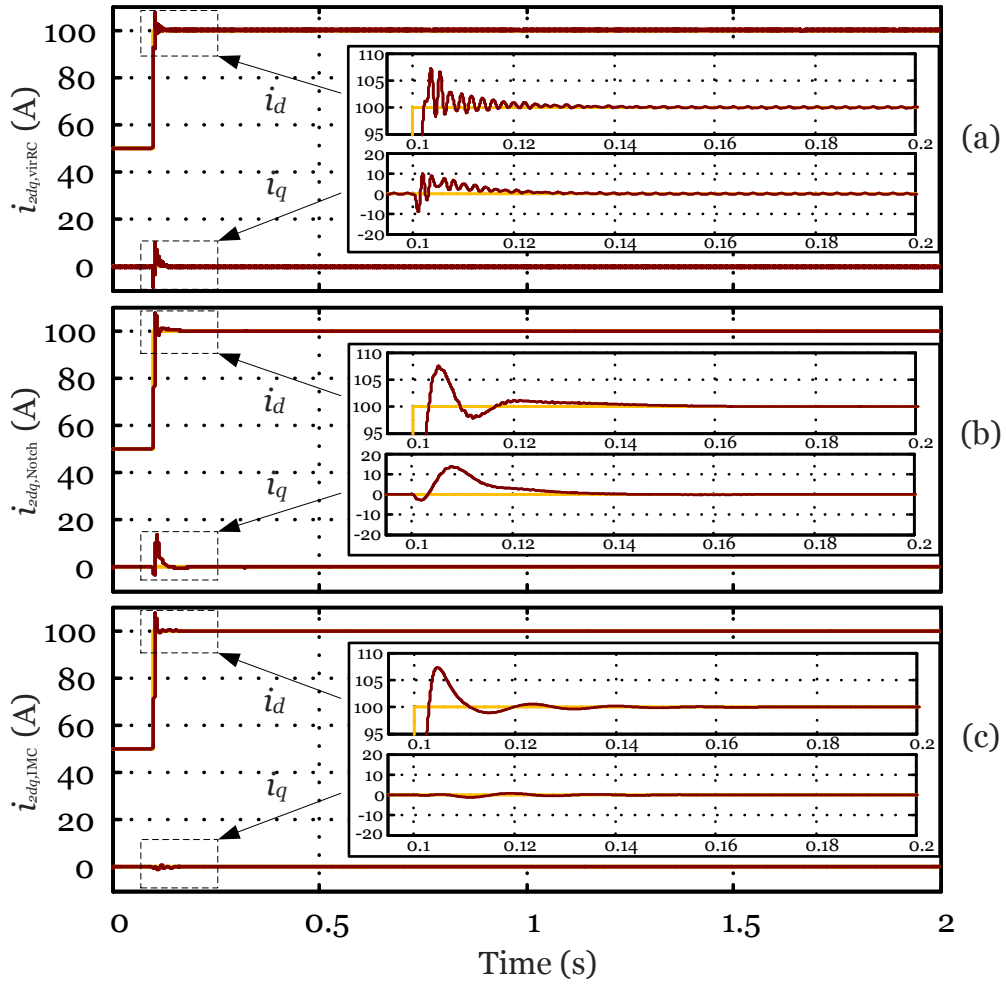

Figure 11.1: dq-components of the current i_2 subsequent to a 50 A step change in the d-component at $t = 0.1$ s: (a) virtual RC, (b) notch filter, and (c) IMC.

All three methods successfully track the new operating state, having settling times of around 20 ms and d-component overshoots of around 7%. As the insets show, the virtual RC method exhibits small decaying transient oscillations in both d and q axes, while the notch filter and the IMC-based methods show smooth transitions. Notice that the IMC-based method exhibits very good decoupling between the d and q axes, having a q-component overshoot of 2%, while the virtual RC and notch filter approachs have q-component overshoots of 10% and 14%, respectively.

Fig. 11.2 shows the corresponding injected three-phase currents i_{2abc} for the three tested methods.

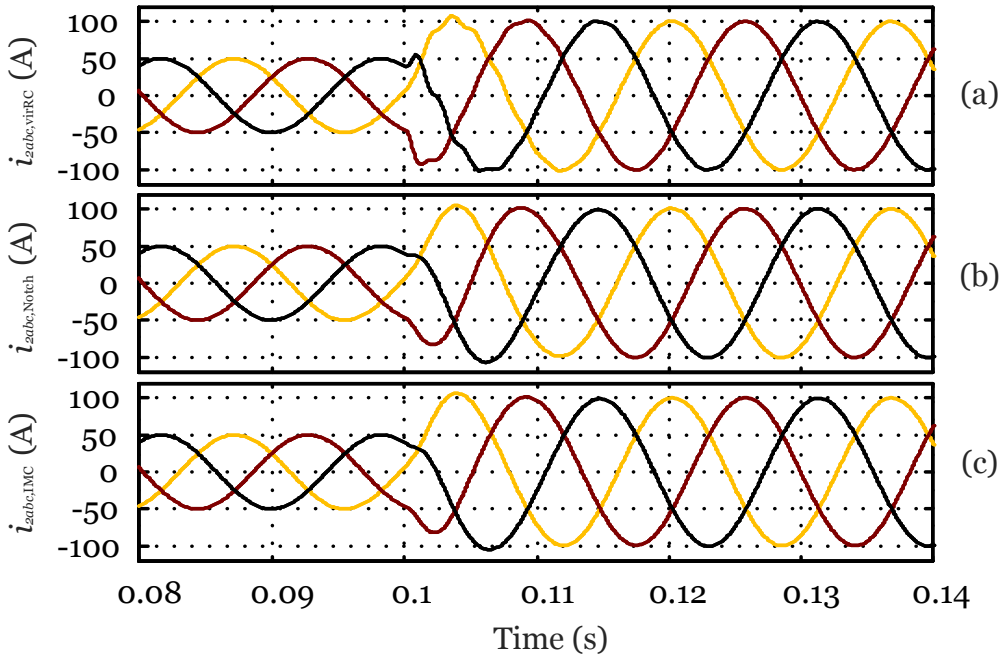

Figure 11.2: Three-phase currents i_{2abc} subsequent to a 50 A step change in the d-component at $t = 0.1$ s: (a) virtual RC, (b) notch filter, and (c) IMC.

Again, the notch filter and the IMC-based methods show smooth transitions, while the virtual RC method has short decaying oscillations, agreeing with what is seen in Fig. 11.1(a).

11.2 Filter Robustness

This section studies the robustness of these three active damping approaches against filter parameter changes that alter the resonance frequency (see Equation 8.1) due to, e.g., heat or aging. The inductance L_2 is increased step by step and the behavior of the three methods is studied (alternatively, the inductance L_1 or the filter capacitance C_f could be changed). THD values are provided in Table 11.1.

Table 11.1: Steady State THD_{63} Values for L_2 Changes

L_2 (mH)	virtual RC	notch filter	IMC
9.6	0.64	1.10	0.82
14.5	unstable	unstable	4.04

As mentioned in Section 10.2, the notch filter is designed to be able to withstand parameter changes that cause a resonance frequency shift of 10%. It is expected that beyond this limit, the transient response of the notch filter–based damping method degrades significantly.

Fig. 11.3 shows the dq-currents of the three methods when L_2 is 9.6 mH (the design value is 1.8 mH) and a 50 A step change in the d-component of the current is applied.

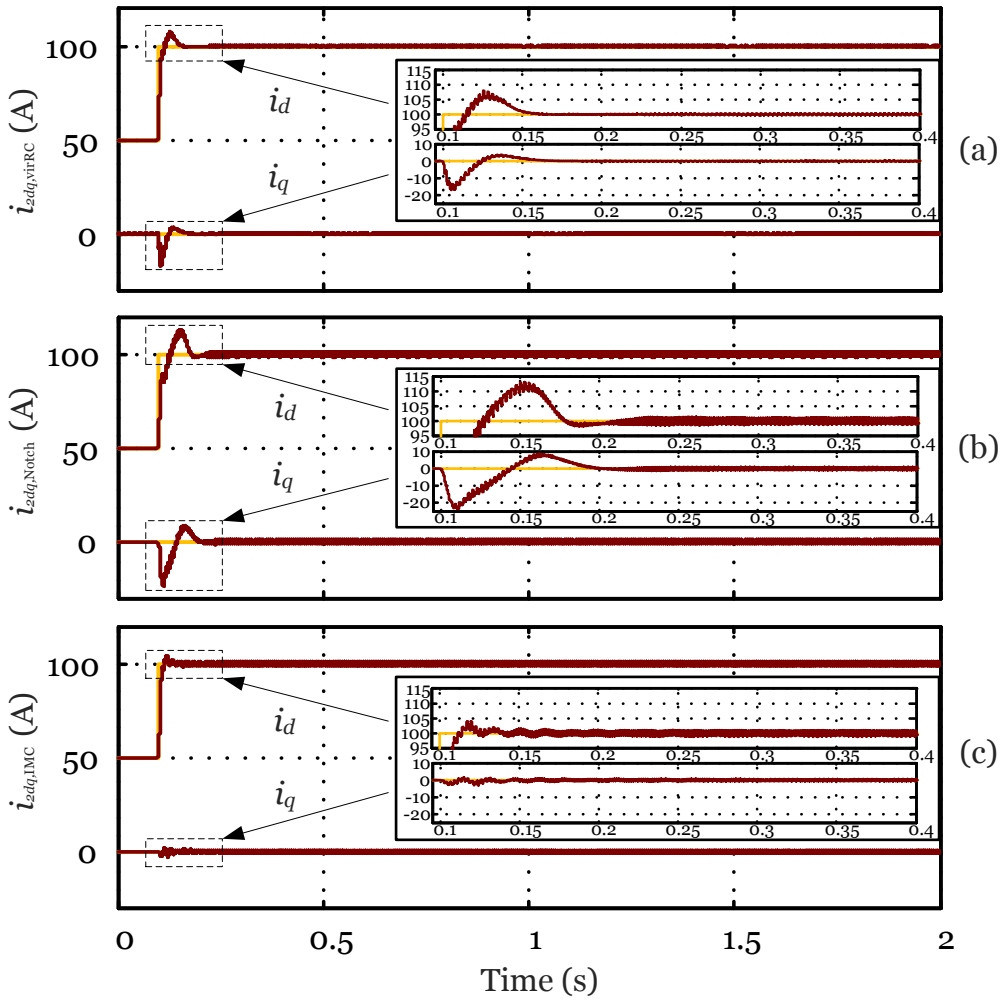

Figure 11.3: dq-components of the current i_2 subsequent to a 50 A step change in the d-component at $t = 0.1$ s for $L_2 = 9.6$ mH: (a) virtual RC, (b) notch filter, and (c) IMC.

With this value of L_2, the robustness limit of the notch filter method is reached as the resonance frequency is shifted to lower frequencies by 10% of its original value, i.e., 540 rad/s. All three methods show steady state oscillations in d and q axes (see Table 11.1 for corresponding THD values).

The virtual RC method has the lowest THD value but the transients in Fig. 11.3(a) slightly degrade compared to Fig. 11.1(a), having a settling time of 50 ms and dq-overshoots of 8% and 17.5%, respectively. The transient response of the notch filter–based approach in Fig. 11.3(b) clearly degrades compared to Fig. 11.1(b), having a settling time of 75 ms and dq-overshoots of 13% and 24%, respectively. This behavior

is expected, as the notch filter is designed for a robustness of 10% [58]. However, the transient behavior of the proposed IMC-based method does not significantly degrade and is still very fast with a small overshoot and very good axes decoupling (settling time of 25 ms and dq-overshoots of 4% and 3%, respectively).

For $L_2 < 9.6$ mH, the transient behavior of the currents is similar to that in Fig. 11.1 but shows small steady state oscillations. Once the value of L_2 is in the neighborhood of the robustness limit of the notch filter method, its transient performance degrades significantly. Increasing L_2 even further increases the THD value and leads to instability of the notch filter method.

Fig. 11.4 shows the three-phase currents i_{2abc} when L_2 is 9.6 mH.

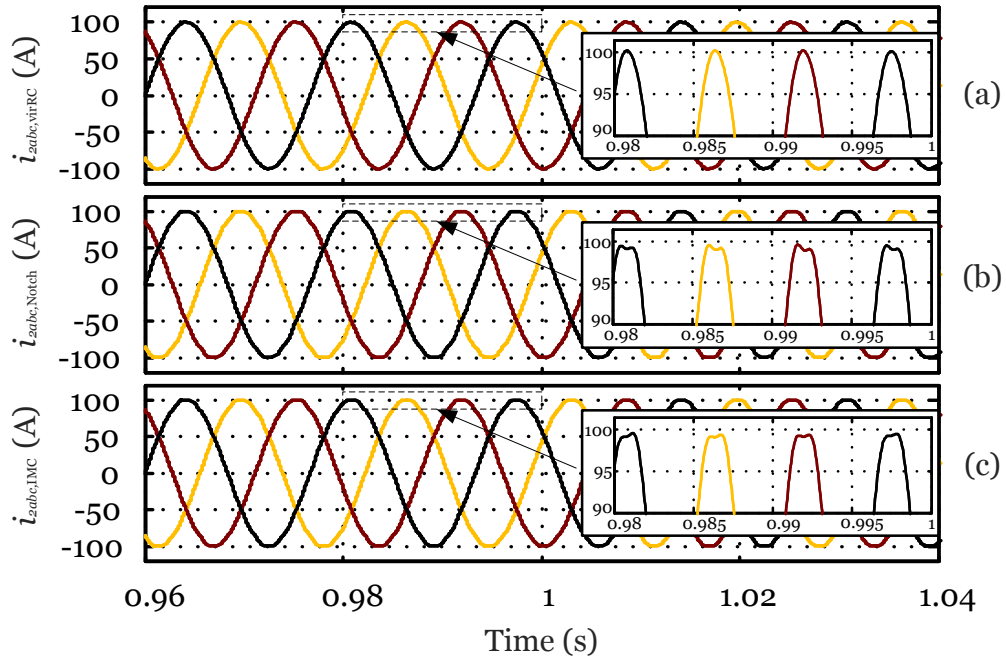

Figure 11.4: Steady state three-phase currents i_{2abc} subsequent to a 50 A step change in the d-component at $t = 0.1$ s for $L_2 = 9.6$ mH: (a) virtual RC, (b) notch filter, and (c) IMC.

As can be seen, all three methods are stable but the current waveforms show distortions in their peaks (also see Table 11.1 for corresponding THD values).

In the next step, L_2 is further increased to 14.5 mH. As shown in Figs. 11.5(a) and (b), the virtual *RC* and notch filter damping methods lose tracking ability, leading to instability (the L_2 stability limit is around 12 mH for virtual *RC* damping and around 10 mH for the notch filter approach).

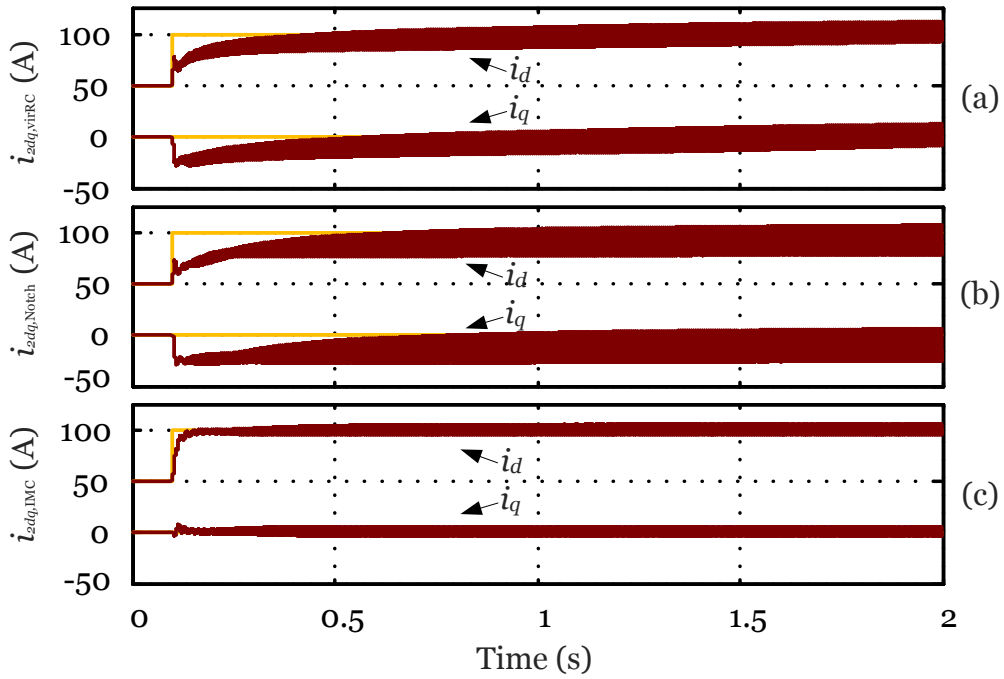

Figure 11.5: *dq*-components of the current i_2 subsequent to a 50 A step change in the *d*-component at $t = 0.1$ s for $L_2 = 14.5$ mH: (a) virtual *RC*, (b) notch filter, and (c) IMC.

Notice that for $L_2 = 14.5$ mH, the proposed IMC-based method (see Fig. 11.5(c)) still retains stability, showing mild oscillations in *d* and *q* axes (its stability limit is around 14.7 mH with a THD value of 4.56%). The IMC-based method is much more stable than both virtual *RC* and notch filter damping methods.

Fig. 11.6 shows the steady state three-phase current waveforms i_{2abc} of the IMC-based method.

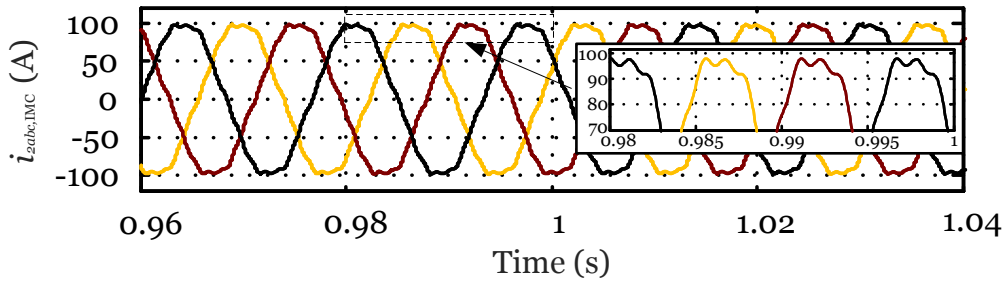

Figure 11.6: Three-phase currents i_{2abc} subsequent to a 50 A step change in the d-component at $t = 0.1$ s for $L_2 = 14.5$ mH using IMC method.

The waveforms show distortion; however, the THD value of 4.04% (also see Table 11.1) is below the 5% limit [64] of the *IEEE* standard 1547 and hence still acceptable.

11.3 Grid Connection Robustness

This subsection studies the behavior of the IMC controller in situations of a weak grid connection (large coupling inductor, e.g., long transmission line). Owing to changes of switching states in the grid, L_g can change during operation which alters the resonance frequency Equation 8.1. Therefore, L_g is successively increased and the behavior of the three controllers is studied.

Fig. 11.7 shows the dq-currents of all three methods when L_g is increased from 2.5 mH to 8.7 mH.

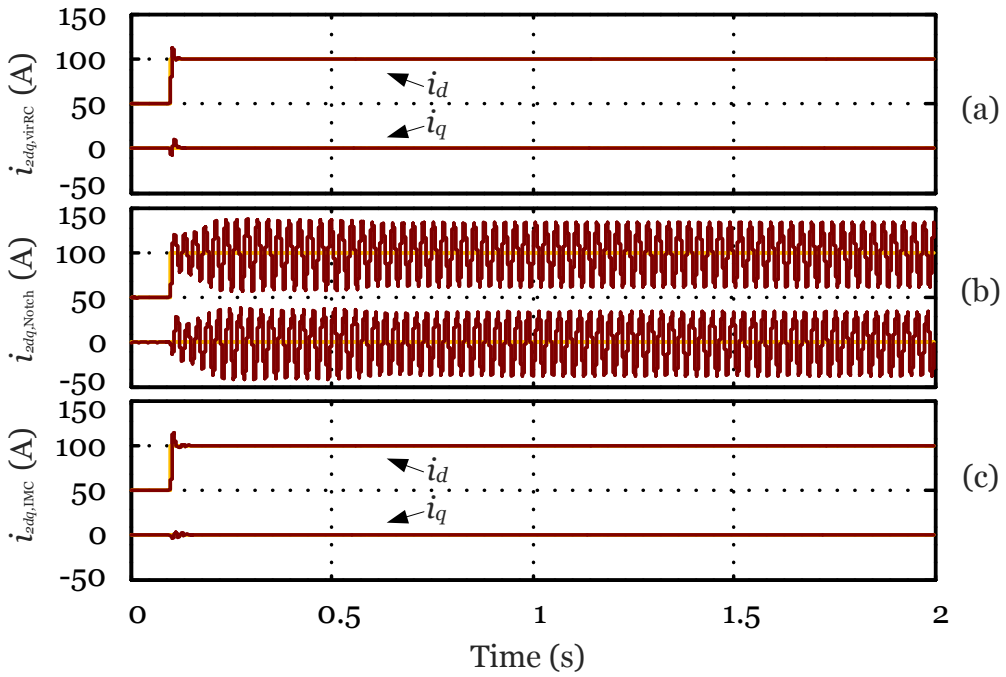

Figure 11.7: dq-components of the current i_2 subsequent to a 50 A step change in the d-component at t = 0.1 s for L_g = 8.7 mH: (a) virtual RC, (b) notch filter, and (c) IMC.

As can be seen, the notch filter approach shows large oscillations in the d and q axes, while the virtual RC and the proposed IMC-based approaches show very robust behavior and no steady state oscillations. For $L_g \geq 8.7$ mH, the oscillations of the notch filter approach become larger and cause instability eventually.

Fig. 11.8 shows the corresponding steady state three-phase currents of all three methods.

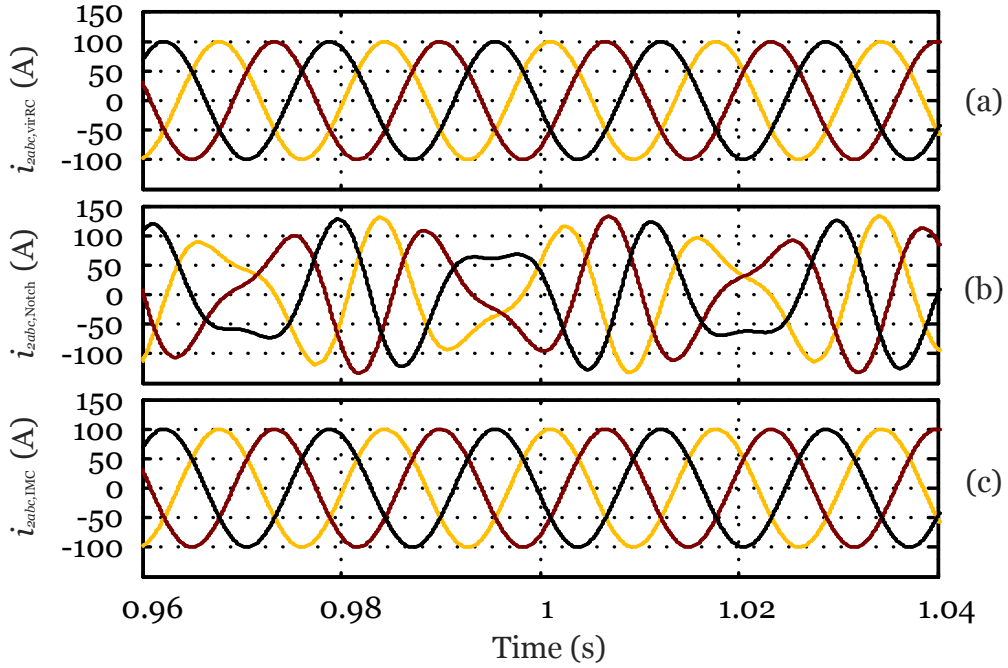

Figure 11.8: Steady state three-phase currents i_{2abc} subsequent to a 50 A step change in the d-component at $t = 0.1$ s for $L_g = 8.7$ mH: (a) virtual RC, (b) notch filter, and (c) IMC.

While the virtual RC and IMC-based approaches show no harmonic distortion, the notch filter approach has large distortion with a THD value of around 40% (see Table 11.2).

Table 11.2: Steady State THD_{63} Values for L_g Changes

L_g (mH)	virtual RC	notch filter	IMC
8.7	0	40	0
10.057	0	unstable	0
10.0925	unstable	unstable	0

Figs. 11.9(a) and (b) show the L_g stability limits of the virtual *RC* and IMC damping methods, i.e., 10.057 mH for the virtual *RC* damping and 10.0925 mH for the proposed IMC-based method.

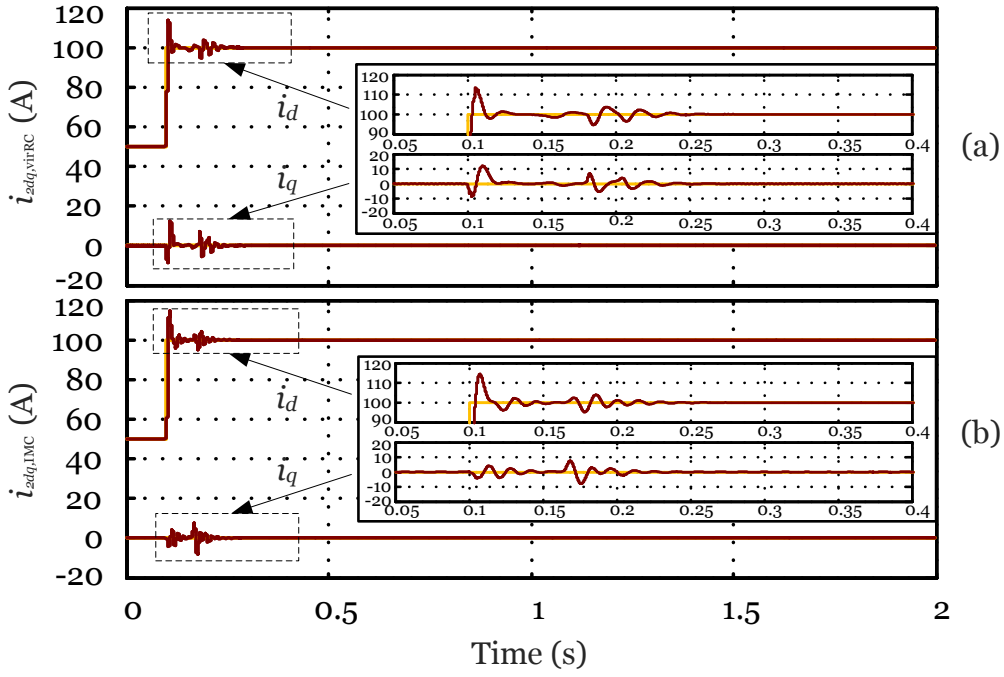

Figure 11.9: *dq*-components of the current i_2 subsequent to a 50 A step change in the *d*-component at t = 0.1 s: (a) virtual *RC* (L_g = 10.057 mH) and (b) IMC (L_g = 10.0925 mH).

The proposed method is slightly more stable than the virtual *RC* damping. However, a further increase in L_g causes instability for both approaches.

Chapter 12

Conclusion Part III

High-order filter–based active damping techniques (e.g., notch filters) are effective in damping the resonance of LCL filters but lack robustness. They are designed to compensate the resonance peak of the LCL filter and take some robustness into account, which compromises bandwidth. The notch filter approach requires separate tuning of the PI controllers and the notch filters which are particularly hard to tune as information about the resonance peak magnitude a_{peak} is required. Additional feedback active damping approaches (e.g., virtual RC) are usually more robust than filter-based once but they need additional sensors. The virtual RC method requires separate tuning of the PI controllers and high-pass filters.

Part III of this thesis proposes an internal model control (IMC)-based active damping approach. The IMC-based controller is essentially a high-order MIMO filter which combines the advantages of both filter-based and additional feedback–based active damping methods. It does not require extra sensors (like the notch filter approach) and has better robustness than the virtual RC method. Moreover, the transient response of the IMC controller hardly degrades when parameters are changed, while the compared methods show large overshoots and might violate current limitations. Although the IMC controller has higher complexity, it is very easy to tune as it has only one tuning parameter. Due to the easy tuning and high robustness, the proposed IMC-based active damping method is superior to both the virtual RC and notch filter methods.

Future Work

In the process of writing this thesis, several research directions for future studies emerged and are listed below:

Part II

1. For the sake of simplicity, the voltage source converters of the study microgrid in Part II do not take switching into account and are essentially controlled ideal voltage sources. For future studies, switching actions of the voltage source converters should be considered.

2. The used power controller utilizes conventional droop control. The internal model–based controllers could be studied with other power sharing approaches, e.g., VPD/FQB, complex line impedance–based droop control, angle droop control, voltage-current droop control [65], or washout filter–based power sharing [43, 66].

3. A practical implementation of the internal model–based voltage and current controllers in the voltage source converters of a physical islanded microgrid would be necessary to confirm the time-domain simulation case studies.

4. Future studies could also investigate the behavior of the IMC-based voltage and current controllers in case of non-linear loads and/or highly resistive lines in a low-voltage microgrid.

Part III

1. The proposed IMC-based active damping controller is studied for a single grid-connected voltage source converter with LCL filter. As the next step, it would be interesting to study multiple grid-connected LCL-filtered voltage source

converters in parallel to study multi-resonance phenomenons as pointed out in [50, 60].

2. Also, an experimental implementation of the proposed IMC-based active damping controller would be necessary to confirm the time-domain simulation case studies.

3. The proposed active damping controller is designed for grid-connected VSCs with LCL filters. It would be interesting to develop an IMC-based voltage regulator for LCL-filtered voltage source converters in an islanded microgrid.

4. The discussed resonance problem could also be tackled by an active disturbance rejection–based approach utilizing state observers.

Bibliography

[1] M. Yazdanian and A. Mehrizi-Sani, "Internal model–based current control of the RL filter-based voltage-sourced converter," *IEEE Trans. Energy Convers.*, vol. 29, no. 4, pp. 873–881, Dec. 2014.

[2] ——, "Case studies on cascade voltage control of islanded microgrids based on the internal model control," in *9th IFAC Symp. Control of Power and Energy Syst. (CPES)*, New Delhi, India, Dec. 2015.

[3] ——, "Internal model–based voltage control of a standalone distributed generator," *IEEE Trans. Energy Convers.*, submitted for review (paper no. TEC-00402-2016), May 2016.

[4] S. Leitner, M. Yazdanian, A. Mehrizi-Sani, and A. Muetze, "Small-signal stability analysis of an inverter-based microgrid with internal model–based controllers," *IEEE Trans. Power Syst.*, submitted for review, May 2016.

[5] ——, "Internal model–based active damping current control for a grid-connected voltage source converter with an LCL-filter," *IEEE Trans. Power Del.*, submitted for review, Oct. 2016.

[6] R. H. Lasseter, "Microgrids," in *IEEE Power Eng. Soc. Winter Meeting*, vol. 1, 2002, pp. 305–308.

[7] F. Katiraei, R. Iravani, N. Hatziargyriou, and A. Dimeas, "Microgrids management," *IEEE Power Energy Mag.*, vol. 6, no. 3, pp. 54–65, May 2008.

[8] A. L. Dimeas and N. D. Hatziargyriou, "Operation of a multiagent system for microgrid control," *IEEE Trans. Power Syst.*, vol. 20, no. 3, pp. 1447–1455, Aug. 2005.

[9] F. Katiraei and M. R. Iravani, "Power management strategies for a microgrid with multiple distributed generation units," *IEEE Trans. Power Syst.*, vol. 21, no. 4, pp. 1821–1831, Nov. 2006.

[10] N. Pogaku, M. Prodanovic, and T. C. Green, "Modeling, analysis and testing of autonomous operation of an inverter-based microgrid," *IEEE Trans. Power Electron.*, vol. 22, no. 2, pp. 613–625, Mar. 2007.

[11] A. Bidram and A. Davoudi, "Hierarchical structure of microgrids control system," *IEEE Trans. Smart Grid*, vol. 3, no. 4, pp. 1963–1976, Dec. 2012.

[12] J. A. P. Lopes, C. L. Moreira, and A. G. Madureira, "Defining control strategies for microgrids islanded operation," *IEEE Trans. Power Syst.*, vol. 21, no. 2, pp. 916–924, May 2006.

[13] R. Majumder, B. Chaudhuri, A. Ghosh, R. Majumder, G. Ledwich, and F. Zare, "Improvement of stability and load sharing in an autonomous microgrid using supplementary droop control loop," *IEEE Trans. Power Syst.*, vol. 25, no. 2, pp. 796–808, May 2010.

[14] M. S. Mahmoud and F. M. AL-Sunni, *Control and Optimization of Distributed Generation Systems*. Springer International Publishing, 2015.

[15] Open electrical. [Online]. Available: http://www.openelectrical.org/wiki/index.php?title=Dq0_Transform

[16] M. J. Gibbard, P. Pourbeik, and D. J. Vowles, *Small-signal stability, control and dynamic performance of power systems*. University of Adelaide Press, Adelaide, 2015.

[17] P. Kundur, *Power system stability and control*. New York: McGraw-Hill, 1994.

[18] S. Saxena and Y. V. Hote, "Load frequency control in power systems via internal model control scheme and model-order reduction," *IEEE Trans. Power Syst.*, vol. 28, no. 3, pp. 2749–2757, Aug. 2013.

[19] W. Tan, "Unified tuning of PID load frequency controller for power systems via IMC," *IEEE Trans. Power Syst.*, vol. 25, no. 1, pp. 341–350, Feb. 2010.

[20] F. Alonge, F. D'Ippolito, and T. Cangemi, "Identification and robust control of DC/DC converter hammerstein model," *IEEE Trans. Power Electron.*, vol. 23, no. 6, pp. 2990–3003, Nov. 2008.

[21] C. Xia, Y. Yan, P. Song, and T. Shi, "Voltage disturbance rejection for matrix converter-based PMSM drive system using internal model control," *IEEE Trans. Ind. Electron.*, vol. 59, no. 1, pp. 361–372, Jan. 2012.

[22] G. Liu, L. Chen, W. Zhao, Y. Jiang, and L. Qu, "Internal model control of permanent magnet synchronous motor using support vector machine generalized inverse," *IEEE Trans. Ind. Informat.*, vol. 9, no. 2, pp. 890–898, May 2013.

[23] K. C. Wong, S. L. Ho, and K. W. E. Cheng, "Direct control algorithm for doubly fed induction generators in weak grids," *IET Electric Power Applications*, vol. 3, no. 4, pp. 371–380, Jul. 2009.

[24] L. Harnefors and H. P. Nee, "Model-based current control of AC machines using the internal model control method," *IEEE Trans. Ind. Appl.*, vol. 34, no. 1, pp. 133–141, Jan. 1998.

[25] D. Campos-Gaona, E. L. Moreno-Goytia, and O. Anaya-Lara, "Fault ride-through improvement of DFIG-WT by integrating a two-degrees-of-freedom internal model control," *IEEE Trans. Ind. Electron.*, vol. 60, no. 3, pp. 1133–1145, Mar. 2013.

[26] C. E. Garcia and M. Morari, "Internal model control. A unifying review and some new results," *Ind. Eng. Chem. Proc. Des. Dev.*, vol. 21, no. 2, pp. 308–323, Apr. 1982.

[27] D. E. Rivera, M. Morari, and S. Skogestad, "Internal model control: PID controller design," *Ind. Eng. Chem. Proc. Des. Dev.*, vol. 25, no. 1, pp. 252–265, 1986.

[28] M. Yazdanian and A. Mehrizi-Sani, "Distributed control techniques in microgrids," *IEEE Trans. Smart Grid*, vol. 5, no. 6, pp. 2901–2909, Nov. 2014.

[29] D. Olivares, A. Mehrizi-Sani, A. Etemadi, C. Canizares, R. Iravani, M. Kazerani, A. Hajimiragha, O. Gomis-Bellmunt, M. Saeedifard, R. Palma-Behnke, G. Jimenez-Estevez, and N. Hatziargyriou, "Trends in microgrid control," *IEEE Trans. Smart Grid*, vol. 5, no. 4, pp. 1905–1919, Jul. 2014.

[30] J. M. Carrasco, L. G. Franquelo, J. T. Bialasiewicz, E. Galvan, R. C. P. Guisado, M. A. M. Prats, J. I. Leon, and N. Moreno-Alfonso, "Power-electronic systems for the grid integration of renewable energy sources: A survey," *IEEE Trans. Ind. Electron.*, vol. 53, no. 4, pp. 1002–1016, Jun. 2006.

[31] Y. Li, D. M. Vilathgamuwa, and P. C. Loh, "Design, analysis, and real-time testing of a controller for multibus microgrid system," *IEEE Trans. Power Electron.*, vol. 19, no. 5, pp. 1195–1204, Sep. 2004.

[32] C. K. Sao and P. W. Lehn, "Control and power management of converter fed microgrids," *IEEE Trans. Power Syst.*, vol. 23, no. 3, pp. 1088–1098, Aug. 2008.

[33] B. Kroposki, C. Pink, R. DeBlasio, H. Thomas, M. Simoes, and P. K. Sen, "Benefits of power electronic interfaces for distributed energy systems," *IEEE Trans. Energy Convers.*, vol. 25, no. 3, pp. 901–908, Sep. 2010.

[34] C. Schauder and H. Mehta, "Vector analysis and control of advanced static VAr compensators," *IEE Proc. Gener. Transm. Distrib.*, vol. 140, no. 4, pp. 299–306, Jul. 1993.

[35] P. G. Barbosa, L. G. B. Rolim, E. H. Watanabe, and R. Hanitsch, "Control strategy for grid-connected DC-AC converters with load power factor correction," *IEE Proc. Gener. Transm. Distrib.*, vol. 145, no. 5, pp. 487–491, Sep. 1998.

[36] A. Yazdani and R. Iravani, "A unified dynamic model and control for the voltage-sourced converter under unbalanced grid conditions," *IEEE Trans. Power Del.*, vol. 21, no. 3, pp. 1620–1629, Jul. 2006.

[37] B. Bahrani, S. Kenzelmann, and A. Rufer, "Multivariable-PI-based *dq* current control of voltage source converters with superior axis decoupling capability," *IEEE Trans. Ind. Electron.*, vol. 58, no. 7, pp. 3016–3026, Jul. 2011.

[38] A. Mehrizi-Sani and R. Iravani, "Online set point modulation to enhance microgrid dynamic response: Theoretical foundation," *IEEE Trans. Power Syst.*, vol. 27, no. 4, pp. 2167–2174, Nov. 2012.

[39] ——, "Online set point adjustment for trajectory shaping in microgrid applications," *IEEE Trans. Power Syst.*, vol. 27, no. 1, pp. 216–223, Feb. 2012.

[40] F. Katiraei and M. R. Iravani, "Power management strategies for a microgrid with multiple distributed generation units," *IEEE Trans. Power Syst.*, vol. 21, no. 4, pp. 1821–1831, Nov. 2006.

[41] I. R. Yazdani A., *Voltage-Sourced Converters in Power Systems: Modeling, Control, and Applications*. Wiley, 2010.

[42] A. Yazdani, "Control of an islanded distributed energy resource unit with load compensating feed-forward," in *Power and Energy Society General Meeting - Conversion and Delivery of Electrical Energy in the 21st Century, 2008 IEEE*, Jul. 2008, pp. 1–7.

[43] M. Yazdanian, S. Leitner, A. Mehrizi-Sani, and A. Muetze, "Small-signal analysis and power sharing properties of washout filter-based power controllers," *IEEE Trans. Power Syst.*, submitted for review (paper no. TPWRS-00946-2016), Jun. 2016.

[44] J. M. Uudrill, "Dynamic stability calculations for an arbitrary number of interconnected synchronous machines," *IEEE Trans. Power App. Syst.*, vol. PAS-87, no. 3, pp. 835–844, Mar. 1968.

[45] S. S. Damodhar and S. Krishna, "Comparison of participation factor method and selective eigenvalue computation for voltage stability analysis," in *8th Mediterranean Conf. Power Gen. Transm. Distrib. and Energy Convers. (MEDPOWER 2012)*, Oct. 2012, pp. 1–6.

[46] J. M. Carrasco, L. G. Franquelo, J. T. Bialasiewicz, E. Galvan, R. C. PortilloGuisado, M. A. M. Prats, J. I. Leon, and N. Moreno-Alfonso, "Power-electronic systems for the grid integration of renewable energy sources: A survey," *IEEE Trans. Ind. Electron.*, vol. 53, no. 4, pp. 1002–1016, Jun. 2006.

[47] E. Twining and D. G. Holmes, "Grid current regulation of a three-phase voltage source inverter with an LCL input filter," *IEEE Trans. Power Electron.*, vol. 18, no. 3, pp. 888–895, May 2003.

[48] M. Liserre, F. Blaabjerg, and S. Hansen, "Design and control of an LCL-filter-based three-phase active rectifier," *IEEE Trans. Ind. Appl.*, vol. 41, no. 5, pp. 1281–1291, Sep. 2005.

[49] J. Dannehl, C. Wessels, and F. W. Fuchs, "Limitations of voltage-oriented PI current control of grid-connected PWM rectifiers with LCL filters," *IEEE Trans. Ind. Electron.*, vol. 56, no. 2, pp. 380–388, Feb. 2009.

[50] I. Lorzadeh, M. Savaghebi, H. A. Abyaneh, and J. M. Guerrero, "Active damping techniques for LCL-filtered inverters-based microgrids," in *Diagnostics for Electrical Machines, Power Electronics and Drives (SDEMPED), 2015 IEEE 10th International Symposium on*, Sep. 2015, pp. 408–414.

[51] M. Malinowski and S. Bernet, "A simple voltage sensorless active damping scheme for three-phase PWM converters with an LCL filter," *IEEE Trans. Ind. Electron.*, vol. 55, no. 4, pp. 1876–1880, Apr. 2008.

[52] P. A. Dahono, "A control method for DC-DC converter that has an LCL output filter based on new virtual capacitor and resistor concepts," in *Power Electronics Specialists Conference, 2004. PESC 04. 2004 IEEE 35th Annual*, vol. 1, Jun. 2004, pp. 36–42 Vol.1.

[53] J. Dannehl, F. W. Fuchs, S. Hansen, and P. B. Thogersen, "Investigation of active damping approaches for PI-based current control of grid-connected pulse width modulation converters with LCL filters," *IEEE Trans. Ind. Appl.*, vol. 46, no. 4, pp. 1509–1517, Jul. 2010.

[54] R. Pena-Alzola, M. Liserre, F. Blaabjerg, R. Sebastian, J. Dannehl, and F. W. Fuchs, "Systematic design of the lead-lag network method for active damping in LCL-filter based three phase converters," *IEEE Trans. Ind. Informat.*, vol. 10, no. 1, pp. 43–52, Feb. 2014.

[55] X. Wang, F. Blaabjerg, and P. C. Loh, "Virtual RC damping of LCL-filtered voltage source converters with extended selective harmonic compensation," *IEEE Trans. Power Electron.*, vol. 30, no. 9, pp. 4726–4737, Sep. 2015.

[56] S. Mariethoz and M. Morari, "Explicit model-predictive control of a PWM inverter with an LCL filter," *IEEE Trans. Ind. Electron.*, vol. 56, no. 2, pp. 389–399, Feb. 2009.

[57] M. Liserre, R. Teodorescu, and F. Blaabjerg, "Stability of photovoltaic and wind turbine grid-connected inverters for a large set of grid impedance values," *IEEE Trans. Power Electron.*, vol. 21, no. 1, pp. 263–272, Jan. 2006.

[58] J. Dannehl, M. Liserre, and F. W. Fuchs, "Filter-based active damping of voltage source converters with LCL filter," *IEEE Trans. Ind. Electron.*, vol. 58, no. 8, pp. 3623–3633, Aug. 2011.

[59] S. Zhang, S. Jiang, X. Lu, B. Ge, and F. Z. Peng, "Resonance issues and damping techniques for grid-connected inverters with long transmission cable," *IEEE Trans. Power Electron.*, vol. 29, no. 1, pp. 110–120, Jan. 2014.

[60] X. Lu, K. S. L. Huang, and M. L. F. Blaabjerg, "An active damping method based on biquad digital filter for parallel grid-interfacing inverters with LCL filters," in *2014 IEEE Applied Power Electronics Conference and Exposition - APEC 2014*, Mar. 2014, pp. 392–397.

[61] C. P. Dick, S. Richter, M. Rosekeit, J. Rolink, and R. W. D. Doncker, "Active damping of LCL resonance with minimum sensor effort by means of a digital infinite impulse response filter," in *Power Electronics and Applications, 2007 European Conference on*, Sep. 2007, pp. 1–8.

[62] B. Bahrani, S. Kenzelmann, and A. Rufer, "Multivariable-PI-based *dq* current control of voltage source converters with superior axis decoupling capability," *IEEE Trans. Ind. Electron.*, vol. 58, no. 7, pp. 3016–3026, Jul. 2011.

[63] D. Schröder, *Elektrische Antriebe - Regelung von Antriebssystemen*. Springer-Verlag Berlin Heidelberg, 2009.

[64] *IEEE Standard for Interconnecting Distributed Resources With Electric Power Systems*, IEEE15471, 2005.

[65] M. S. Golsorkhi and D. D. C. Lu, "A control method for inverter-based islanded microgrids based on V-I droop characteristics," *IEEE Trans. Power Del.*, vol. 30, no. 3, pp. 1196–1204, June 2015.

[66] M. Yazdanian and A. Mehrizi-Sani, "Washout filter–based power sharing," *IEEE Trans. Smart Grid*, vol. 7, no. 2, pp. 967–968, Mar. 2016.

List of figures

List of tables